Hydromechanical coupling in unsaturated clayey rocks with double porosity based on a multiscale homogenization procedure

Sabrina C.Y. Ip[1] · Ronaldo I. Borja[1,*]

[1]Department of Civil and Environmental Engineering, Stanford University, Stanford, CA 94305, USA. *E-mail: borja@stanford.edu

Summary. Shales and clay rocks are porous media with multiscale microstructures used in many engineering applications. Intact clay rocks often exhibit a bimodal pore size distribution in which the nanopores are related to the interlayer spacing in the clay platelet and the micropores are related to the interparticle pores between clay particles. The double-porosity microstructure has significant implications for the hydromechanical behavior of these rocks especially in unsaturated conditions. In this study, we develop a double-porosity hydromechanical framework incorporating a homogenization scheme to simulate fluid flow and elastic deformation in anisotropic clay rocks. The homogenization scheme provides an enriched description of the elastic behavior of clay rocks during changes in the degree of saturation by bridging the nano, micro, and macroscale characterizations. We also model the nanopores and micropores as two independent pore networks with distinct fluid flow mechanisms and permeabilities. The proposed framework is cast into a three-field mixed finite element formulation for solving fully coupled flow and deformation problems. Numerical examples of free and confined swelling in Opalinus clay samples are presented to demonstrate the impacts of a multiscale microstructure on wetting processes in clay rocks.

Keywords. Anisotropy, double porosity, micromechanics, poroelasticity, unsaturated rock mechanics

1 Introduction

Shales and clayey rocks have been identified as promising geomaterials for a variety of applications, including as host rocks for nuclear waste repositories [108], as source rocks of low-carbon fuels [86], and as cap rocks of potential geological formations for hydrogen storage and CO_2 sequestration [60, 111]. Many of these applications involve two-phase fluid transport along with changes in the degree of saturation. Due to their high clay content, many shales are highly susceptible to swelling and shrinkage when they undergo a

change of saturation, which can alter their permeability, strength and elastic moduli [1, 10, 28, 40, 51, 85, 97, 99, 158]. Shale swelling and its associated material property changes can have severe consequences including wellbore instability and loss of caprock integrity. As such, there is a need for a fundamental understanding of complex hydromechanical behaviors in clay-rich shales and clayey rocks, and modeling methods for predicting shale swelling.

A major factor influencing swelling behavior is the shale's multiscale microstructure [146]. Shale can be considered to have the following microstructure in order of increasing magnitude: (1) elementary clay platelets at the nanoscopic scale, (2) elementary clay platelets stacked together to form clay particles, (3) an assembly of clay particles forming a clay matrix at the submicrometer scale, (4) the clay matrix intermixed with detrital grains (mainly quartz and calcite) at the submillimeter scale, and (5) alternating clay-rich and detrital layers resulting in depositional layering [16, 26, 132]. Consequently, shale has pore sizes that span multiple orders of magnitude. Most pores in the shale's matrix have an average radius ranging from 1–200 nm [76, 93]. The pores can be classified into intraparticle and interparticle pores depending on their sizes (nanometer vs micron) [94]. The majority of pores in the shale matrix are intraparticle pores (with radii ranging from 3–6 nm), but most of the pore volume is contributed from the larger interparticle pores (with radii larger than 100 nm) [37]. Intact shale can thus be modeled as a double porosity medium [35, 54, 106, 148] in which the micropores are related to the interlayer spacing in the clay platelet, and the macropores are related to the interparticle pores. We differentiate this from fractured shales that often have fractures (in the order of millimeters or larger) that can dominate the flow behavior [38, 52, 54], which are not covered in the present discussion.

Several modeling approaches have been developed to account for fluid flow in porous media with complex pore structure spanning multiple scales, including discrete fracture models [34, 79, 102, 109], multi-porosity models [9, 55], and equivalent continuum models [14, 112]. Dual porosity models are a subset of multi-porosity models where the two pore regions are considered as individual continua that exist within the same solid matrix. The pore regions interact with each other through local exchange of fluids in response to a pressure head gradient. Notably, dual porosity models can be preferable to discrete fracture models, which explicitly model all the micro-fractures in the medium of interest, as they are less computationally prohibitive and do not require explicit representation of the fracture distribution and patterns [13]. Simultaneously, dual porosity models are often more representative of double porosity systems than equivalent continuum models which describe the double porous material as a single homogenous medium. The balance between model simplification and calculation precision thus makes dual porosity models favorable for field-scale modeling [4]. A number of studies have developed hydromechanical dual-porosity and dual-permeability frameworks [7, 15, 56, 82, 83, 134, 154, 155]. Some of these models have been extended to the case of double porous media with two immiscible fluids [19, 21, 32, 33, 89, 120].

The microstructure of shale also influences its material properties. Many shales exhibit transverse isotropy in either or both deformation and fluid flow behavior [22, 61, 122, 165, 167], mainly due to preferred orientation of clay platelets and pores along distinct bedding planes. The shale microstructure can also evolve upon a change in the degree of saturation [151, 153] and result in changes to the mechanical properties [25, 57, 145, 147, 162] as well as the degree of elastic and plastic anisotropy [42, 71–73, 88, 121, 133, 151, 153]. Several studies have developed microstructure-informed constitutive models and investigated the impact of shale's multiscale microstructure on its mechanical properties using analytical homogenization schemes [26, 41, 44–46, 74] and numerical upscaling techniques [59, 113, 161]. Cariou et al. [26] addressed the multiscale microstructure of unsaturated Callovo-Oxfordian shale using a three-level homogenization model. Ip and Borja [74] also formulated a multiscale model to capture evolving anisotropic elastic moduli in clayey rocks upon wetting and drying. Eghbalian et al. [45, 46] formulated multiscale models for capturing the swelling behavior of poroelastic and poroelastoplastic clayey materials. Recently, Alaoui et al. [2] implemented a multiscale constitutive law into a single porosity hydromechanical framework. However, none of the aforementioned constitutive models have been implemented in a dual porosity framework. Only a handful of hydromechanical dual porosity models have accounted for anisotropic mechanical and hydraulic properties [156, 157, 159, 163], but these studies do not explicitly consider the rock's microstructure.

In this study, a dual-porosity hydromechanical model is developed based on the multiscale microstructure of shales. The multiscale homogenization model introduced in Ip and Borja [74] is first reviewed, with an extension to the evolution of nano and microscale porosities. Using analytical homogenization techniques, the lower-scale strains are upscaled to derive the macroscale governing equations and obtain the relevant poroelastic coefficients for an unsaturated double-porosity poroelastic medium. We note that while shales can exhibit plastic strains during wetting and drying processes [73, 162], it is beyond the scope of this study. To the authors' knowledge, this is the first time the governing equations of a dual-porosity model have been developed from a multiscale constitutive law. The remaining constitutive laws for fluid flow in the nano and micropores, and mass transfer between the nanopores and micropores are then discussed. Subsequently, the proposed framework is cast into a three-field mixed finite element formulation for solving fully coupled flow and deformation problems. Numerical examples of free and confined swelling of Opalinus clay are presented to demonstrate the impacts of a multiscale microstructure and double porosity on drying and wetting processes in shales.

2 Mechanistic background

We consider the unsaturated double-porosity medium as a mixture of a solid phase, micropores (interparticle pores) and nanopores (intraparticle pores). The pore spaces may be filled by liquid and/or gas, assumed to be water and air, respectively. In the following section, s, m, and M represent the solid, nanopores, and micropores, respectively; while a and w represent the air and water phases, respectively.

The volume fractions $\phi^{\alpha\beta}$ of the three phases $\beta = s, m, M$ must follow the closure condition

$$\phi^s + \sum_{\alpha=w,a} \sum_{\beta=m,M} \phi^{\alpha\beta} = 1\,. \tag{1}$$

The total porosity of the medium ϕ is simply

$$\phi = \sum_{\alpha=w,a} \sum_{\beta=m,M} \phi^{\alpha\beta} = 1 - \phi^s\,. \tag{2}$$

The pore fractions are defined as the ratio between the pore volume occupied by a porous phase $\beta = m, M$ in relation to the total volume of the pores, and are given by

$$\psi^\beta = \frac{\phi^\beta}{1-\phi^s}, \quad \phi^\beta = \sum_{\alpha=w,a} \phi^{\alpha\beta}\,, \tag{3}$$

with the following closure condition

$$\psi^M + \psi^m = 1\,. \tag{4}$$

Next, we assume that the pore spaces are filled with a mixture of water and air. The local saturation of fluid α in porous phase β is given by the relation

$$S^{\alpha\beta} = \frac{\phi^{\alpha\beta}}{\phi^\beta} = \frac{\phi^{\alpha\beta}}{\psi^\beta(1-\phi^s)}\ . \tag{5}$$

while the total saturation of phase β in the porous material is

$$\bar{S}^\beta = \psi^M S^{M\beta} + \psi^m S^{m\beta}\,, \tag{6}$$

For simplicity, we assume the pore water to be incompressible and the pore air pressure to be zero (i.e., atmospheric). The governing equations for a variably saturated double porosity medium include the balance of linear momentum for the mixture and the balance of mass for the pore water in the macropores and micropores. The balance of linear momentum can be expressed as [17, 18, 163],

$$\nabla \cdot \boldsymbol{\sigma} + \rho \boldsymbol{g} = \bar{\boldsymbol{c}}\,, \tag{7}$$

where $\boldsymbol{\sigma}$ is the total Cauchy stress tensor and ρ is the total mass density of the mixture, given by

$$\rho = (1-\phi)\rho_s + (\phi^{wm} + \phi^{wM})\rho_w \,. \tag{8}$$

In the above equation, ρ_s and ρ_w are the intrinsic mass densities of solid and water, respectively (mass of air is ignored) and $\boldsymbol{g}$ is the acceleration vector. The term $\bar{\boldsymbol{c}}$ is the momentum produced by the fluid mass transfer between the two pore scales, which takes the form

$$\bar{\boldsymbol{c}} = \sum_{\beta=m,M} c^{\beta} \tilde{\boldsymbol{v}}_{\beta} \,, \tag{9}$$

where c^{β} are the water mass transfer terms that satisfy the closure condition $c^M + c^m = 0$ and $\tilde{\boldsymbol{v}}_{\beta}$ is the relative velocity of pore water in porous phase β with respect to the solid phase.

The balance of mass for fluid α contained in submixture β may be written in terms of the material time derivative with respect to the solid motion [19],

$$\dot{\phi}^{\alpha\beta} + \frac{\phi^{\alpha\beta}}{K_\alpha}\dot{p}_\beta + \phi^{\alpha\beta}\nabla\cdot\boldsymbol{v} = \frac{c_{\alpha\beta}}{\rho_\alpha} - \frac{1}{K_\alpha}\nabla p_\beta \cdot \boldsymbol{q}_{\alpha\beta} - \nabla\cdot\boldsymbol{q}_{\alpha\beta} \,, \tag{10}$$

With the help of Equation (5), the first term in Equation (10) can be expanded as

$$S^{\alpha\beta}\dot{\phi}^{\beta} + \phi^{\beta}\dot{S}^{\alpha\beta} + \frac{\phi^{\alpha\beta}}{K_\alpha}\dot{p}_\beta + \phi^{\alpha\beta}\nabla\cdot\boldsymbol{v} = \frac{c_{\alpha\beta}}{\rho_\alpha} - \frac{1}{K_\alpha}\nabla p_\beta \cdot \boldsymbol{q}_{\alpha\beta} - \nabla\cdot\boldsymbol{q}_{\alpha\beta} \,, \tag{11}$$

Building on the three-scale upscaling scheme detailed in Ip and Borja [74], we derive the balance of mass equations for an unsaturated double porosity medium comprising clay particles (with nanopores), micropores, and inclusions. While Ip and Borja [74] also introduced microcracks in their constitutive model, we assume in this study that the rock has no microcracks for simplicity.

To this end, we first introduce the theorems that allow us to upscale the strain fields $\boldsymbol{\varepsilon}^i$ from the nanoscale to the macroscale, where $i = n, \mu, m, M$ represent the nanoscale, microscale, mesoscale and macroscale, respectively. We consider a REV in the domain Ω comprising multiple material phases β, each assumed to have homogeneous properties. In the following subsections, the matrix (solid) phases are denoted by superscript s and the pore spaces are denoted by superscript p. The

$$\boldsymbol{\sigma} = \mathbb{C}(\boldsymbol{x}) : \boldsymbol{\epsilon} + \boldsymbol{\sigma}_p(\boldsymbol{x}) \,, \tag{12}$$

where $\boldsymbol{\sigma}$ is the heterogeneous stress tensor in the REV, $\boldsymbol{\epsilon}$ is the heterogeneous strain tensor in the REV, $\boldsymbol{\sigma}_p$ is the local eigenstress tensor, and $\boldsymbol{x}$ is the position vector in Ω.

Using Levin's theorem [87], the average stress in the REV can be written as

$$\boldsymbol{\Sigma} = \mathbb{C}^{hom} : \boldsymbol{E} + \boldsymbol{\Sigma}_p \,, \tag{13}$$

where $\mathbb{C}^{hom} = \overline{\mathbb{C} : \mathbb{A}}$ is the homogenized stiffness tensor, $\boldsymbol{\Sigma}_p = \overline{\boldsymbol{\sigma}_p : \mathbb{A}}$ is the homogenized eigenstress, $\boldsymbol{\Sigma}^n$ is the homogenized stress tensor, $\boldsymbol{E}^n$ is the homogenized strain tensor, $\mathbb{A}$ is the strain concentration tensor, and $\overline{(\cdot)}$ represents the volume average.

The local strains in material phase α caused in the REV by the homogenized strain tensor can be expressed as [43, 116]

$$\boldsymbol{\varepsilon}^\alpha = \mathbb{A}^\alpha : \boldsymbol{E} + \sum_\beta \mathbb{B}^{\alpha\beta} : \mathbb{C}^{\beta\,-1} : \varsigma^\beta \,, \tag{14}$$

where $\mathbb{B}^{\alpha\beta}$ is the eigenstrain influence tensor. We simplify the notation going forward by representing $\bar{\mathbb{B}}^{\alpha\beta} = \mathbb{B}^{\alpha\beta} : \mathbb{C}^{\beta\,-1}$. Specific expressions for $\bar{\mathbb{B}}$ are provided in Appendix A.

In this study, we adopt a Mori-Tanaka homogenization scheme [63, 104], where the averaged concentration tensors in phase i $(i = s, p)$ can be expressed as:

$$\mathbb{A}^i = (\mathbb{I} + \mathbb{P} : (\mathbb{C}^i - \mathbb{C}^s))^{-1} : \overline{(\mathbb{I} + \mathbb{P} : (\mathbb{C} - \mathbb{C}^s))^{-1}}^{-1} \,, \tag{15}$$

where $\mathbb{P}$ is the Hill tensor that depends on the matrix properties and the shape and orientation of the inclusions [47]. The Mori-Tanaka homogenization scheme adopted in the proposed model has been shown to provide consistent results regardless of the type of boundary condition applied (uniform stress or uniform strain) [107] and has been used to upscale the material properties in porous media [44, 45, 58]. We note that while the self-consistent approach has been shown to be more precise when the volume fraction of inclusions is high [96], it is a nonlinear scheme that requires an iterative procedure to calculate the strain concentration tensor. As a result, adopting the self-consistent scheme would significantly increase simulation run times and the computational power required.

3 Homogenization procedure

We briefly review the three-scale upscaling model presented in Ip and Borja [74] starting with the nanoscale. The homogenization model only accounts for elastic deformation. Plastic deformation will be investigated in a future study.

3.1 Microstructure of clayey rocks

The microstructure of clayey rocks are span multiple scales and are integral to understanding their mechanical and hydraulic properties. At the micron scale, the microstructure of these rocks comprises isolated non-clayey mineral

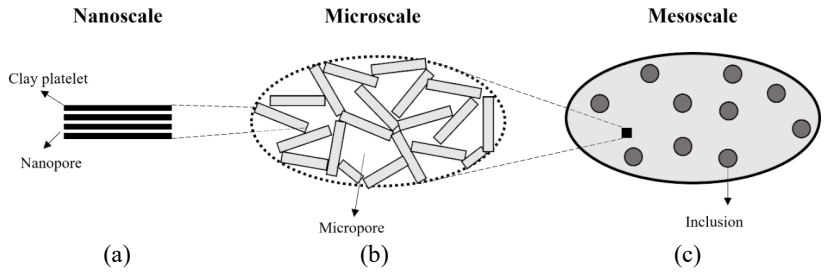

Fig. 1. Three-step homogenization model incorporating the microstructure of clay rocks. (a) Nanoscale: clay particle comprising clay platelets and nanopores; (b) Microscale: Assembly of clay particles and micropores; (c) Macroscale: Clay matrix surrounding inclusions (Adapted from Ip and Borja [74]).

grains distributed within a fine-grained clay matrix [81]. The mineral grains are often isolated from one another within the matrix with grain diameters ranging from 10-30 μm [115]. Cracks are also often observed in samples at this scale [115], however we do not consider them in this study. Within the clay matrix, the clay particles observed are generally smaller than 2 μm and are oriented preferentially along the bedding plane. There exists small elongated pores between similarly oriented clay particles and crescent shaped pores that occur between folded sheets of clay that are aligned with the bedding plane [70, 80, 115]. We refer to the pores at this scale as micropores. At the nanoscale, the clay particles consist of stacks of clay platelets that are locally aligned [69, 130]. The space between platelets is usually called the interlayer space and is filled with water molecules and counterions. We refer to these pores as nanopores. At the micron scale, clayey rocks can thus be ideally represented by a double porosity medium comprising nanopores and micropores.

3.2 Clay platelet $\rightarrow$ Nanoscale

Ip and Borja [74] idealized a clay particle as multiple layers of parallel clay platelets with interlayer spaces in between each platelet (Figure 1(a)). The interlayer space is always filled with interlayer water ($S^{mw} = 1$, $\dot{S}^{mw} = 0$) and exchangeable cations, which results in mechanical, hydraulic, and electrochemical forces being present. The clay platelets are assumed to be incompressible ($\nu \rightarrow 0.5$).

The forces in the interlayer water can be described with the Gouy-Chapman double layer theory [29, 101]. There is an electrical potential distribution around the clay platelets that arises from their negative surface charge interacting with the exchangeable cations in the pore fluid. The electrical potential distributions of two clay platelets interact as they approach each other, resulting in a repulsive double layer force in the interlayer space that depends on the interlayer distance, the ionic concentration, and the ionic valence. The

double layer force per unit area between two parallel clay platelets has been derived as [75, 84, 101]

$$\pi^{\mathrm{DDL}} = 2nkT(\cosh(u) - 1)\,, \tag{16}$$

where

$$u = 8\tanh^{-1}\Big(\exp(-\kappa h)\tanh(\frac{z}{4})\Big)\,, \tag{17a}$$

$$\kappa = \sqrt{\frac{2nv^2e'^2}{\varepsilon kT}}\,, \tag{17b}$$

$$z = 2\sinh^{-1}\Big(\frac{\mathrm{CEC}}{\mathrm{SSA}}\sqrt{\frac{1}{8\epsilon nkT}}\Big)\,, \tag{17c}$$

CEC is the cation exchange capacity, SSA is the specific surface of the clay platelet, ε is the static permittivity of the water solution, n is the ion concentration in the pore water, k is the Boltzmann constant (1.38×10^{-23} J/K), T is the absolute temperature (assumed to be 293.15 K), e' is the electric charge (1.602×10^{-19} C), and v is the ionic valence. In this study, we assume constant values of $v = 1$, CEC = 0.732 mEq/g, and $\varepsilon = 7.083 \times 10^{-10}$ C^2/(J · m) [69, 84]. We also note that the ionic concentration is assumed to remain constant throughout the drying process and geochemically-induced shrinkage is not considered in this work.

In addition to the double layer forces, it is well known that attractive van der Waals forces exist between two molecules in close distance to each other. Similar to the double layer force, this attractive force increases with decreasing interlayer distance. The van der Waals force for two parallel layers [27, 84] was derived from London's theory for the attractive stress between two molecules [92] and is given by

$$\pi^{\mathrm{VDW}} = \frac{A_h}{24\pi}\Big(\frac{1}{(h/2)^3} + \frac{1}{(h/2+t)^3} - \frac{2}{(h/2+t/2)^3}\Big)\,, \tag{18}$$

where t is the thickness of the clay mineral crystals, which we assume to be 0.96 nm, and A_h is the Hamaker constant, which has a value of 2.2×10^{-21} J for montmorillonite from theoretical analysis of coagulation measurements [110].

Since the interlayer space remains fully saturated, the stress in the interlayer water can be described by a liquid pressure p_m and an overpressure π acting in the normal direction to the clay platelets $\boldsymbol{n}$ [26, 45]:

$$\boldsymbol{\sigma}^f = -p_m\mathbf{1} - \pi\boldsymbol{n}\otimes\boldsymbol{n}\,,\ \pi = \pi^{\mathrm{DDL}} - \pi^{\mathrm{VDW}}. \tag{19}$$

Using a first-order Taylor's series expansion and defining the fluid strain as $\boldsymbol{\varepsilon}^{nf} = dh/h_0\boldsymbol{n}\otimes\boldsymbol{n}$, we can write a constitutive law for the interlayer water as

$$\delta\boldsymbol{\sigma}^p = \mathbb{C}^p : \delta\boldsymbol{\varepsilon}^p + \delta\boldsymbol{\sigma}^p_p\,, \tag{20}$$

where

$$\mathbb{C}^p = -h_0 K^p \boldsymbol{n}\otimes\boldsymbol{n}\otimes\boldsymbol{n}\otimes\boldsymbol{n}, \quad K^p = \frac{\partial\pi}{\partial h}\Big|_{h_0+\delta h/2,n_0}, \tag{21a}$$

$$\delta\boldsymbol{\sigma}^p = -\delta p_m \mathbf{1} - \delta\pi \boldsymbol{n}\otimes\boldsymbol{n}, \quad \delta\pi = \pi\Big|_{h_0,n} - \pi\Big|_{h_0,n_0}, \tag{21b}$$

h_0 is the interlayer distance in the initial configuration, and n is the ionic concentration in the initial configuration.

By idealizing the interlayer spaces as oblate spheroids with small aspect ratio, ξ, that tends to 0 ($\xi \to 0$), the following homogenized stiffness of the clay particle can be obtained [44]

$$[\mathbb{C}^n] = \begin{bmatrix} c_1 & c_3 & c_4 & 0 & 0 & 0 \\ \cdot & c_1 & c_4 & 0 & 0 & 0 \\ \cdot & \cdot & c_2 & 0 & 0 & 0 \\ 0 & 0 & 0 & 0 & 0 & 0 \\ 0 & 0 & 0 & 0 & 0 & 0 \\ 0 & 0 & 0 & 0 & 0 & 2c_5 \end{bmatrix}, \tag{22}$$

where

$$c_1 = \frac{1-\phi^n}{\phi^n}(K^p - K^p\phi^n + 4\mu\phi^n), \tag{23a}$$

$$c_2 = \frac{K^p}{\phi^n}, \tag{23b}$$

$$c_3 = \frac{1-\phi^n}{\phi^n}(K^p - K^p\phi^n + 2\mu\phi^n), \tag{23c}$$

$$c_4 = K^p(\frac{1}{\phi^n} - 1), \tag{23d}$$

$$c_5 = (1-\phi^n)\mu, \tag{23e}$$

μ is the shear modulus of the clay platelets, and ϕ^n is the porosity at the nanoscale. We note that the shear stiffness of the clay particle in the parallel direction is 0 since the platelets can slide over each other. The prestress of the clay particle can be expressed as [26, 45]

$$\delta\boldsymbol{\Sigma}_p^n = -\delta p_m \mathbf{1} - \delta\pi(\mathbf{1} - \phi^n(\mathbf{1} - \boldsymbol{n}\otimes\boldsymbol{n})). \tag{24}$$

Under certain loading conditions, the interlayer water can transition from a liquid-like phase to a solid-like phase that is associated with stick-slip friction behavior among the clay platelets [78]. The internal sliding friction is postulated to follow a Mohr-Coulomb failure criterion [98].

The porosity in the nanoscale REV can be written as

$$\phi^n = \frac{V^{np}}{V^{np} + V^{ns}} \tag{25}$$

and its overall change is

$$\dot{\phi}^n = (1 - \phi^n)\phi^n \mathbf{1} : \dot{\boldsymbol{\varepsilon}}^{np} \,, \tag{26}$$

where V^{np} and V^{ns} are the volumes of the nanopores and clay platelets in the REV, respectively.

Since the clay platelets are assumed to be incompressible, $\mathbf{1} : \dot{\boldsymbol{\varepsilon}}^{nm} = 0$, and so, upscaling of the nanoscale strains is simply

$$\mathbf{1} : \dot{\boldsymbol{\varepsilon}}^{np} = \frac{1}{\phi^n} \mathbf{1} : \dot{\boldsymbol{\varepsilon}}^{\mu m} \,. \tag{27}$$

Equation (26) can thus be expressed as

$$\dot{\phi}^n = (1 - \phi^n) \mathbf{1} : \dot{\boldsymbol{\varepsilon}}^{\mu m} \,. \tag{28}$$

3.3 Nanoscale → Microscale

At the microscale, the REV comprises an assembly of clay particles and a network of interparticle pores, herein referred to as micropores. The clay particles are preferentially oriented along the bedding plane [39, 69, 95, 124, 138, 141], while the micropores are assumed to be oblate spheroids perfectly aligned with the bedding plane [127, 136, 137]. The micropore network is partially saturated by the same pore fluid as the nanopores. However, the pore fluids at the nanoscale and microscale may not be in equilibrium, and as such, we introduce the micropore water pressure p_M^w and micropore air pressure p_M^a. At this scale, electrostatic and van der Waals forces are negligible and clay particles interact with one another through mechanical forces. As such, the clay matrix can be modeled as a granular medium in which plasticity arises from sliding of clay particles against one another and normal compression between clay particles [46, 150]. Both the Drucker-Prager [62, 125] and the Mohr-Coulomb [46] criteria have been previously adopted to describe the plastic behavior of the clay matrix.

The effective stiffness and effective prestress of the clay particles aligned with respect to the bedding plane can be obtained from the following integral

$$\mathbb{C}^{av} = \frac{1}{8\pi^2} \int_0^{2\pi} \int_0^{2\pi} \int_0^{\pi} \mathrm{ODF}(\tilde{\theta}) \mathbb{C}^{\mathrm{n}}(\tilde{\theta}, \tilde{\psi}, \tilde{\phi}) \sin(\tilde{\theta}) \, \mathrm{d}\tilde{\theta} \, \mathrm{d}\tilde{\psi} \, \mathrm{d}\tilde{\phi} \,, \tag{29a}$$

$$\delta \boldsymbol{\Sigma}_p^{av} = -\delta p_m \mathbf{1} - \delta\pi \boldsymbol{\tau} \,, \tag{29b}$$

$$\boldsymbol{\tau} = \Big((1 - \phi^n) \mathbf{1} + \phi^n \frac{1}{8\pi^2} \int_0^{2\pi} \int_0^{2\pi} \int_0^{\pi} \mathrm{ODF}(\tilde{\theta}) \boldsymbol{n} \otimes \boldsymbol{n} \sin(\tilde{\theta}) \, \mathrm{d}\tilde{\theta} \, \mathrm{d}\tilde{\psi} \, \mathrm{d}\tilde{\phi} \Big) \,, \tag{29c}$$

where $\tilde{\theta}$, $\tilde{\psi}$ and $\tilde{\phi}$ are Euler angles [114], and ODF is the Owens-March orientation distribution function [95]

$$\mathrm{ODF}(\tilde{\theta}) = \frac{\mathrm{MPD}}{(\cos^2(\tilde{\theta}) + \mathrm{MPD}\sin^2(\tilde{\theta}))^{1.5}}\,. \tag{30}$$

MPD is the maximum pole density, a parameter measured in logarithmic scale from 1.0 to ∞ with MPD = 1.0 for a random distribution of clay particles and MPD = ∞ for perfectly aligned clay particles.

We consider the micropore geometry to be oblate spheroids with an aspect ratio $\xi = l_{min}/l_{max}$, where l_{min} and l_{max} are the minimum and maximum principal radii, respectively. Depending on the size of the micropores, they can be either saturated with water or air. As a result, there exist surface tension stresses at the interfaces, $\gamma^{\alpha\beta}$, where $\alpha\beta = s, w, a$ represent the solid, water and air phases. The membrane stress tensor can be expressed as [26, 45]

$$\omega^{\alpha\beta} = \gamma^{\alpha\beta}(\mathbf{1} - \hat{\boldsymbol{n}} \otimes \hat{\boldsymbol{n}})\,, \tag{31}$$

where $\hat{\boldsymbol{n}}$ is the unit normal vector at a point on the interface between two phases [30, 31].

The state equation of the clay matrix can then be written as

$$\mathbb{C}^{\mu} = \begin{cases} \mathbb{C}^{av} \\ \mathbb{O} \\ \mathbb{O} \\ \mathbb{O} \end{cases}, \quad \boldsymbol{\sigma}_p^{\mu} = \begin{cases} \boldsymbol{\sigma}_0^{matrix} + \boldsymbol{\Sigma}_p^{av} & \text{in} \quad \Omega^{\mathrm{matrix}} \\ -p_M^w \mathbf{1} & \text{in} \quad \Omega^{\mathrm{w}} \\ -p_M^a \mathbf{1} & \text{in} \quad \Omega^{\mathrm{a}} \\ \omega^{\alpha\beta} & \text{in} \quad \Gamma^{\alpha\beta} \end{cases}, \tag{32}$$

where $\mathbb{O}$ is a fourth-order null tensor, $\boldsymbol{\sigma}_0^{matrix}$ is the initial prestress in the matrix, and Γ represents the surfaces in the domain between two different phases.

The homogenized macroscopic stiffness and eigenstress of the clay matrix can be obtained using Levin theorem [87] as

$$\mathbb{C}^{\mu} = \mathbb{C}^{av} - \phi^{\mu}\mathbb{C}^{av} : {}^{\mu}\mathbb{A}^{p}\,, \tag{33a}$$

$$\delta\boldsymbol{\Sigma}^{\mu} = -\phi^{\mu}\delta\bar{p}_M\mathbf{1} : {}^{\mu}\mathbb{A}^{p} + (1-\phi^{\mu})\delta\boldsymbol{\Sigma}^{av} : {}^{\mu}\mathbb{A}^{s} + \delta\overline{\omega^{\alpha\beta} : {}^{\mu}\mathbb{A}^{p}}\,, \tag{33b}$$

where ϕ^{μ} is the micropore porosity at the microscale, $\bar{p}_M = S^w p_M^w + (1 - S^w)p_M^a$, and $\mathbb{A}^p$ and $\mathbb{A}^s$ are the strain concentration tensors representing the micropore phase and the clay matrix phase, respectively.

The micropore porosity in the microscale REV can be expressed as

$$\phi^{\mu} = \frac{V^{\mu p}}{V^{\mu p} + V^{np} + V^{ns}}\,, \tag{34}$$

and its overall change is

$$\dot{\phi}^{\mu} = \phi^{\mu}(1-\phi^{\mu})\mathbf{1} : \dot{\boldsymbol{\varepsilon}}^{\mu p} - \phi^{n}\phi^{\mu}(1-\phi^{\mu})\mathbf{1} : \dot{\boldsymbol{\varepsilon}}^{np} \,. \tag{35}$$

where $V^{\mu p}$ is the volume of the micropores in the REV and $\boldsymbol{\varepsilon}^{\mu p}$ is the strain in the micropores at the microscale.

Using Equation (27) and the relationship between strains at the micro- and macroscale,

$$\dot{\boldsymbol{\varepsilon}}^{mm} = (1-\phi^{\mu})\dot{\boldsymbol{\varepsilon}}^{\mu m} + \phi^{\mu}\dot{\boldsymbol{\varepsilon}}^{\mu p} \,, \tag{36}$$

we can rewrite Equation (35) as

$$\dot{\phi}^{\mu} = \phi^{\mu}\mathbf{1} : \dot{\boldsymbol{\varepsilon}}^{\mu p} - \phi^{\mu}\mathbf{1} : \dot{\boldsymbol{\varepsilon}}^{mm} \,. \tag{37}$$

Surface tension contribution

In this study, we adopt the capillary-tube analogy to describe the surface tension in the micropores [26]. The pore network is idealized as a set of oblate spheroids that are fully filled with either water or air. The delineation between these two sets is governed by Laplace relation and the equivalent minimum harmonic mean radius of the pore, $r_{eq} = (0.5(l_{max}^{-1} + (\xi l_{max})^{-1}))^{-1}$. At a given suction, small pores would be filled with water, while water in large pores would have drained and they would be filled with air. The threshold radius can be calculated from the Laplace equation of capillarity as [149]

$$r^{*} = \frac{2\gamma^{lg} cos(\Theta)}{s} \,, \tag{38}$$

where Θ is the contact angle.

Following the derivation of Chateau and Dormieux [30], the surface tension term can be expressed as [26, 45]

$$\overline{\omega^{ab} : \mathbb{A}^{p}} = \phi^{\mu} p^{eq} \boldsymbol{\omega}, \quad \boldsymbol{\omega} = \frac{1}{\Omega^{p}} \int_{\Gamma^{p}} (\mathbf{1} - \hat{\boldsymbol{n}} \otimes \hat{\boldsymbol{n}}) : {}^{\mu}\mathbb{A}^{p} \mathrm{d}\Gamma \,, \tag{39}$$

where p^{eq} is the equivalent pressure in the micropores, defined as

$$p^{eq} = \int_{r_{min}}^{r_{max}} p^{\gamma}(r_{eq}) \mathrm{PSD}(r_{eq}) \, \mathrm{d}r_{eq} \,, \tag{40}$$

r_{min} and r_{max} are the minimum and maximum pore radii, respectively, and PSD is the pore size distribution function, which can be obtained from the water retention curve and

$$p^{\gamma}(r_{eq}) = \begin{cases} 2\gamma^{sl}/r_{eq} & r_{eq} < r^{*} \\ 2\gamma^{sg}/r_{eq} & r_{eq} \geq r^{*} \end{cases} \,. \tag{41}$$

We note that as the pores are spheroidal, analytical integration of the expression for $\hat{\boldsymbol{n}} \otimes \hat{\boldsymbol{n}}$ is complicated and the surface tension is obtained by numerical integration. We assume the solid phase to be perfectly wetting (i.e., $\gamma^{sl} = 0$) and the surface tension between the solid and gas phases and the liquid and gas phases to be equivalent (i.e., $\gamma^{lg} = \gamma^{sg} = 72.5$ mN/m.

3.4 Microscale → Macroscale

Shale and other mudstones often have a significant percentage of inclusions such as quartz and calcite. We upscale an REV that comprises the clay matrix, quartz inclusions, and calcite inclusions. The clay matrix fraction, inclusion fraction and aspect ratio of the inclusions are represented by ϕ^{mat}, ϕ^i and ξ^i, respectively. Once again, the state equation of the shale can be written as:

$$\mathbb{C} = \begin{cases} \mathbb{C}^{\mu} \\ \mathbb{C}^{i} \end{cases}, \quad \boldsymbol{\sigma}_p^M = \begin{cases} \boldsymbol{\sigma}_0 + \boldsymbol{\Sigma}_p^{\mu} & \text{in} \quad \Omega^{\text{matrix}} \\ \boldsymbol{\sigma}_0 & \text{in} \quad \Omega^{\text{i}} \end{cases}, \tag{42}$$

where $\mathbb{C}^i$ is the elasticity tensor for the inclusion phase(s) and $\boldsymbol{\sigma}_0$ is the initial stress in the shale under conditions of no strain and no suction.

Levin theorem gives the homogenized macroscopic stiffness and eigenstress of the shale:

$$\mathbb{C}^M = \mathbb{C}^{\mu} + \phi^i(\mathbb{C}^i - \mathbb{C}^{\mu}) : {}^m\mathbb{A}^i \,, \tag{43a}$$

$$\delta\boldsymbol{\Sigma}_p^M = (1-\phi^i)\delta\boldsymbol{\Sigma}_p^{\mu} : {}^m\mathbb{A}^m \,, \tag{43b}$$

where ${}^m\mathbb{A}^i$ and ${}^m\mathbb{A}^m$ are the strain concentration tensors representing the inclusion phase, and the clay matrix phase, respectively.

The relationship between strains at the mesoscale and macroscale is

$$\dot{\boldsymbol{\varepsilon}}^M = (1-\phi^i)\dot{\boldsymbol{\varepsilon}}^{mm} + \phi^i\dot{\boldsymbol{\varepsilon}}^i \,. \tag{44}$$

The inclusion fraction can be expressed as

$$\phi^i = \frac{V^i}{V^{\mu p} + V^{np} + V^{ns} + V^i} \,, \tag{45}$$

and its evolution as

$$\dot{\phi}^i = \phi^i \mathbf{1} : \dot{\boldsymbol{\varepsilon}}^i - \phi^i \mathbf{1} : \dot{\boldsymbol{\varepsilon}}^M \,, \tag{46}$$

where V^i is the volume of the inclusions in the REV. Using Equations (44) and (46), the evolution of the macroscale matrix volume fraction can be written as

$$\begin{aligned} \dot{\phi}^{mat} &= -\dot{\phi}^i \\ &= (1-\phi^i)(\mathbf{1} : \dot{\boldsymbol{\varepsilon}}^{mm} - \mathbf{1} : \dot{\boldsymbol{\varepsilon}}^M) \,. \end{aligned} \tag{47}$$

At the macroscale, we represent the nanoscale porosity and micro-scale porosity as ϕ^m and ϕ^M, respectively. These variables can be expressed as functions of the lower-scale volume fractions introduced above as

$$\phi^m = \frac{V^{np}}{V^{\mu p} + V^{np} + V^{ns} + V^i} = \phi^n(1-\phi^{\mu})\phi^{mat} \,, \tag{48}$$

$$\phi^M = \frac{V^{\mu p}}{V^{\mu p} + V^{np} + V^{ns} + V^i} = \phi^{\mu}\phi^{mat} \,. \tag{49}$$

With the help of Equations (36) and (44), the evolutions of the porosities at each scale are thus

$$\begin{aligned}\dot{\phi}^m &= (1-\phi^\mu)\phi^{mat}\dot{\phi}^n - \phi^n\phi^{mat}\dot{\phi}^\mu + \phi^n(1-\phi^\mu)\dot{\phi}^{mat} \\ &= \frac{\phi^m}{\phi^n}\mathbf{1}:\dot{\boldsymbol{\varepsilon}}^{\mu m} - \phi^m\mathbf{1}:\dot{\boldsymbol{\varepsilon}}^M\end{aligned} \tag{50}$$

$$\begin{aligned}\dot{\phi}^M &= \phi^{mat}\dot{\phi}^\mu + \phi^\mu\dot{\phi}^{mat}\,, \\ &= \phi^M\mathbf{1}:\dot{\boldsymbol{\varepsilon}}^{\mu p} - \phi^M\mathbf{1}:\dot{\boldsymbol{\varepsilon}}^M\,.\end{aligned} \tag{51}$$

4 Microstructure-informed double porosity formulation

4.1 Conservation laws

Balance of momentum

Using Equation (43b), we can write an incremental effective stress equation at the macroscale as

$$\delta\boldsymbol{\sigma} = \delta\boldsymbol{\sigma}' - \boldsymbol{b}_M\delta\bar{p}_M - \boldsymbol{b}_m\delta p_m - \boldsymbol{b}_\pi\delta\pi + \boldsymbol{b}_\omega\delta p^{eq}\,, \tag{52}$$

where

$$\boldsymbol{b}_M = \phi^M\mathbf{1}:{}^\mu\mathbb{A}^p:{}^m\mathbb{A}^m\,, \tag{53a}$$

$$\boldsymbol{b}_m = \tfrac{\phi^m}{\phi^n}\mathbf{1}:{}^\mu\mathbb{A}^m:{}^m\mathbb{A}^m\,, \tag{53b}$$

$$\boldsymbol{b}_\pi = \tfrac{\phi^m}{\phi^n}\boldsymbol{\tau}:{}^\mu\mathbb{A}^m:{}^m\mathbb{A}^m\,, \tag{53c}$$

$$\boldsymbol{b}_\omega = \phi^M\boldsymbol{\omega}:{}^\mu\mathbb{A}^p:{}^m\mathbb{A}^m\,. \tag{53d}$$

We note the similarity in form to the effective stress derived for clays accounting for physio-chemical effects [26, 45].

The balance of linear momentum equation can then be written as

$$\nabla\cdot\Big(\boldsymbol{\sigma}' - S^w p_M\boldsymbol{b}_M - p_m\boldsymbol{b}_m - \pi\boldsymbol{b}_\pi + p^{eq}\boldsymbol{b}_\omega\Big) + \rho\boldsymbol{g} = \bar{\boldsymbol{c}} \tag{54}$$

Balance of mass

Having obtained the evolutions of the nanoscale and microscale porosities, we can now derive the balance of mass equations for the macroscale REV. Using the strain localization relation, Equation (14), for the microscale and macroscale, and replacing S^{Mw} with S^w, we can rewrite $\dot{\boldsymbol{\varepsilon}}^{\mu m}$ and $\dot{\boldsymbol{\varepsilon}}^{\mu p}$ as:

$$\begin{aligned}\dot{\boldsymbol{\varepsilon}}^{\mu m} =& {}^\mu\mathbb{A}^m:{}^m\mathbb{A}^m:\dot{\boldsymbol{\varepsilon}}^M \\ &+ (\phi^\mu p_M{}^\mu\mathbb{A}^m:{}^m\bar{\mathbb{B}}^{mm}:{}^\mu\mathbb{A}^{p\mathsf{T}}:\mathbf{1} + p_M{}^\mu\bar{\mathbb{B}}^{mp}:\mathbf{1})\dot{S}^w \\ &+ (\phi^\mu S^w{}^\mu\mathbb{A}^m:{}^m\bar{\mathbb{B}}^{mm}:{}^\mu\mathbb{A}^{p\mathsf{T}}:\mathbf{1} + {}^\mu\bar{\mathbb{B}}^{mp}:\mathbf{1})\dot{p}_M \\ &+ ((1-\phi^\mu){}^\mu\mathbb{A}^m:{}^m\bar{\mathbb{B}}^{mm}:{}^\mu\mathbb{A}^{m\mathsf{T}} + {}^\mu\bar{\mathbb{B}}^{mm}):(\dot{p}_m\mathbf{1} + \dot{\pi}\boldsymbol{\tau})\end{aligned} \tag{55}$$

and

$$\begin{aligned}\dot{\boldsymbol{\varepsilon}}^{\mu p} =& {}^{\mu}\mathbb{A}^{p} : {}^{m}\mathbb{A}^{m} : \dot{\boldsymbol{\varepsilon}}^{M} \\ &+ (\phi^{\mu} p_M {}^{\mu}\mathbb{A}^{p} : {}^{m}\bar{\mathbb{B}}^{mm} : {}^{\mu}\mathbb{A}^{p\mathsf{T}} : \mathbf{1} + p_M {}^{\mu}\mathbb{B}^{pp} : \mathbf{1})\dot{S}^{w} \\ &+ (S^{w}\phi^{\mu} {}^{\mu}\mathbb{A}^{p} : {}^{m}\bar{\mathbb{B}}^{mm} : {}^{\mu}\mathbb{A}^{p\mathsf{T}} : \mathbf{1} + {}^{\mu}\bar{\mathbb{B}}^{pp} : \mathbf{1})\dot{p}_M \\ &+ ((1-\phi^{\mu}) {}^{\mu}\mathbb{A}^{p} : {}^{m}\bar{\mathbb{B}}^{mm} : {}^{\mu}\mathbb{A}^{m\mathsf{T}} + {}^{\mu}\bar{\mathbb{B}}^{pm}) : (\dot{p}_m \mathbf{1} + \dot{\pi}\boldsymbol{\tau})\,,\end{aligned} \tag{56}$$

The porosity evolutions in Equations (50) and (51) can then be expanded to

$$\begin{aligned}\dot{\phi^{m}} &= (\boldsymbol{b}_m - \phi^{m}\mathbf{1}) : \dot{\boldsymbol{\varepsilon}}^{M} + \mathcal{C}_m \dot{S}^{w} \\ &\quad + \mathcal{S}_{mM}\dot{p}_M + \boldsymbol{\mathcal{S}}_{mm} : (\dot{p}_m \mathbf{1} + \dot{\pi}\boldsymbol{\tau})\end{aligned} \tag{57}$$

$$\begin{aligned}\dot{\phi^{M}} &= (\boldsymbol{b}_M - \phi^{M}\mathbf{1}) : \dot{\boldsymbol{\varepsilon}}^{M} + \mathcal{C}_M \dot{S}^{w} \\ &\quad + \mathcal{S}_{MM}\dot{p}_M + \boldsymbol{\mathcal{S}}_{Mm} : (\dot{p}_m \mathbf{1} + \dot{\pi}\boldsymbol{\tau})\,.\end{aligned} \tag{58}$$

Specific expressions for $\mathcal{C}_m$, $\tilde{\mathcal{C}}_M$, $\mathcal{S}_{mM}$, $\boldsymbol{\mathcal{S}}_{mm}$, $\tilde{\mathcal{S}}_{MM}$ and $\boldsymbol{\mathcal{S}}_{Mm}$ are presented in Appendix B.

Inserting Equations (57) and (58) into Equation (11) yields the balance of mass for the two porosity scales (micropores and nanopores),

$$\begin{aligned}S^{w}\boldsymbol{b}_M : \dot{\boldsymbol{\varepsilon}} + \mathcal{C}_M \dot{S}^{w} + \mathcal{S}_{MM}\dot{p}_M + \mathcal{S}_{Mm}\dot{p}_m + \mathcal{S}_{M\pi}\dot{\pi} \\ = \frac{c_{wM}}{\rho_w} - \frac{1}{K_w}\nabla p_M \cdot \boldsymbol{q}_{wM} - \nabla \cdot \boldsymbol{q}_{wM}\,,\end{aligned} \tag{59}$$

and

$$\begin{aligned}\boldsymbol{b}_m : \dot{\boldsymbol{\varepsilon}} + \mathcal{C}_m \dot{S}^{w} + \mathcal{S}_{mM}\dot{p}_M + \mathcal{S}_{mm}\dot{p}_m + \mathcal{S}_{m\pi}\dot{\pi} \\ = \frac{c_{wm}}{\rho_w} - \frac{1}{K_w}\nabla p_m \cdot \boldsymbol{q}_{wm} - \nabla \cdot \boldsymbol{q}_{wm}\,,\end{aligned} \tag{60}$$

where $\dot{\boldsymbol{\varepsilon}} = \dot{\boldsymbol{\varepsilon}}^{M}$ and the poroelastic coefficients are

$$\mathcal{S}_{MM} = \frac{S^{w}\phi^{M}}{K_w} + S^{w}\tilde{\mathcal{S}}_{MM}\,, \tag{61a}$$

$$\mathcal{S}_{Mm} = S^{w}\boldsymbol{\mathcal{S}}_{Mm} : \mathbf{1}\,, \tag{61b}$$

$$\mathcal{S}_{mm} = \frac{\phi^{m}}{K_w} + \boldsymbol{\mathcal{S}}_{mm} : \mathbf{1}\,, \tag{61c}$$

$$\mathcal{S}_{M\pi} = \boldsymbol{\mathcal{S}}_{Mm} : \boldsymbol{\tau}\,, \tag{61d}$$

$$\mathcal{S}_{m\pi} = \boldsymbol{\mathcal{S}}_{mm} : \boldsymbol{\tau}\,, \tag{61e}$$

$$\mathcal{C}_M = \phi^{M} + S^{w}\tilde{\mathcal{C}}_M\,. \tag{61f}$$

Appendix C presents the three-field finite element formulation derived from the conservation laws and details the implementation in the Geocentric finite element code [143].

4.2 Constitutive laws

Water retention curve

A water retention law is needed to characterize the relationship between the degree of saturation and the suction. To differentiate between water in the interlayer space and water in the micropores, we adopt a water retention model that includes the effect of bound and capillary water [117]. The water content can be described as the sum of bound and trapped water, θ_a, and capillary water, θ_c, which are functions of the nanopore suction $s_m = -p_m$ and micropore suction $s_M = -p_M$, respectively, i.e.,

$$\theta(s_m, s_M) = \theta_c(s_M) + \theta_a(s_m)\,. \tag{62}$$

The capillary water content is modeled with the van Genuchten retention model [135], while the adsorbed water is modeled with the Freundlich sorption isotherm [53]

$$\theta_c(s_M) = \frac{\theta_{sat} - \theta_a}{\left[1 + (\alpha s_M)^n\right]^{1-1/n}}\,, \tag{63a}$$

$$\theta_a(s_m) = \theta_a^{\max}\Big[\exp\Big(-\frac{M_v}{RT}s_m\Big)\Big]^{1/m_{\text{ads}}}\,, \tag{63b}$$

where α is the inverse of the scaling suction, n is a van Genuchten parameter, m_{ads} is a Freundlich adsorption isoterm coefficient representing the adsorption strength, $\theta_a^{\max}$ is the maximum adsorbed water content, θ_{sat} is the saturated volumetric water content, M_v is the molar volume of water, R is the universal gas constant, and T is the absolute temperature. The micropore degree of saturation and total degree of saturation can then be expressed as

$$S^w(s_m, s_M) = \frac{\theta_c(s_M)}{\theta_{sat} - \theta_a(s_m)}\,, \tag{64a}$$

$$\bar{S}^w(s_m, s_M) = \frac{\theta_c(s_M) + \theta_a(s_m)}{\theta_{sat}}\,. \tag{64b}$$

We note that a water retention curve is used in the proposed model instead of a pore size distribution which has been previously adopted in several studies [2, 45, 46]. The calibrated water retention curve is then used to back-calculate the pore size distribution since water retention curve data is more often measured in swelling tests as compared to direct pore size distribution measurements.

Fluid flow

The proposed model requires two constitutive equations to describe fluid flow in the nanopores and micropores. Modeling fluid flow in multi-porous media,

especially with regards to nanopore flow, is non-trivial and an active area of research. As such, we make simple assumptions about the flow at both scales. Several studies have postulated that Darcy's law is valid to describe the flow in both nanopores and micropores under certain situations [5, 33, 156, 166]. Darcy's law gives the following relationship between $\boldsymbol{q}_{\alpha\beta}$ and p_α at the nanoscale,

$$\boldsymbol{q}_{wm} = -\frac{\boldsymbol{\kappa}_m}{\mu_w} \cdot (\nabla p_m - \rho_w \boldsymbol{g}) \,, \tag{65}$$

and at the microscale,

$$\boldsymbol{q}_{wM} = -\frac{k_{\mathrm{rel}}(S^w) \cdot \boldsymbol{\kappa}_M}{\mu_w} \cdot (\nabla p_M - \rho_w \boldsymbol{g}) \,, \tag{66}$$

where $\boldsymbol{\kappa}_\alpha$ is the intrinsic permeability in pore scale α, $\boldsymbol{k}_{\mathrm{rel}}$ is the relative permeability in the micropores, and μ_w is the dynamic viscosity of the pore fluids.

We consider that the inter-layer water can only flow parallel to the clay platelets. As such, the intrinsic permeability tensor κ_f of the nanopores may be written as

$$\boldsymbol{\kappa}_m = \frac{1}{8\pi^2} \int_0^{2\pi} \int_0^{2\pi} \int_0^{\pi} \mathrm{ODF}(\tilde{\theta}) \kappa_{\mathrm{m},\parallel} (\mathbf{1} - \boldsymbol{n} \otimes \boldsymbol{n}) \sin(\tilde{\theta}) \, \mathrm{d}\tilde{\theta} \, \mathrm{d}\tilde{\psi} \, \mathrm{d}\tilde{\phi} \,. \tag{67}$$

where $\kappa_{m,\parallel}$ is the flow component parallel to the clay platelets. Assuming the flow between the clay platelets can be represented by flow between parallel plates, the permeability parallel to the clay platelets would vary with the interlayer spacing [68, 131, 156]

$$\kappa_{m,\parallel} = \kappa \frac{h^3}{{h_0}^3} \,. \tag{68}$$

where h_0 is the interlayer spacing at the initial condition and κ is the initial clay platelet permeability. We neglect the effects of diffusion and non-linear flow at the nanoscale in this study.

We adopt the van Genuchten-Mualem equation [105, 135] for the relative permeability of the micropores

$$k_{\mathrm{rel}}\left(S^w\right) = {S^w}^{\frac{1}{2}} \left[1 - \left(1 - {S^w}^{1/n} \right)^{1-1/n} \right]^2 . \tag{69}$$

Mass transfer

We consider a first-order mass transfer equation as follows [55]

$$\frac{c_{wM}}{\rho_w} = \bar{k} \frac{\bar{\alpha}}{\mu_w} (p_m - p_M) \,, \tag{70a}$$

$$\frac{c_{wm}}{\rho_w} = \bar{k} \frac{\bar{\alpha}}{\mu_w} (p_M - p_m) \,, \tag{70b}$$

$$\bar{\alpha} = \frac{\bar{\beta}}{\bar{a}^2} \gamma \,, \tag{70c}$$

where $\bar{k}$ is the interface permeability, $\bar{a}$ is the characteristic length of the micropores spacing, β is a dimensionless coefficient accounting for the solid matrix geometry, and γ is a dimensionless scaling coefficient suggested to be 0.4 to fit experimental results [55].

5 Numerical examples

5.1 Free swelling of Opalinus clay

Experimental data demonstrating the anisotropic swelling behavior of shales during free swelling tests are available in the literature. In particular, Minardi et al. [100] presented the anisotropic swelling strains of Opalinus clay samples upon suction variation. They used the vapor equilibrium technique to wet several samples of Opalinus clay from an initial suction of 96 MPa to a final suction of 9.8 MPa while measuring the bed-normal (BN) and bed-parallel (BP) strains, as well as the water content variation. The bedding planes of their samples were perpendicular to the axis of the cylinder.

In this section, we calibrate the model parameters against their swelling test data through free swelling simulations of Opalinus clay. The Opalinus clay sample in the study was a 20 mm-tall cylinder with a diameter of 25 mm. We divided the geometry into a structured mesh with 640 eight-node hexahedral finite elements. The bottom surface was supported on vertical rollers and the center node was fixed for stability. The nanopore and micropore suctions were applied on all surfaces. We present the 3D mesh in Figure 2(a) and a cross-section of the mesh across the sample's diameter on the y-z plane in Figure 2(b).

The parameters of the three-scale homogenization model were calibrated against the anisotropic strains at equilibrium, while the hydraulic parameters were calibrated against the time evolution of the sample's water content. The water retention curve was estimated from the water content data and from observations of the nanopore and micropore fractions reported in Keller et al. [80]. Figure 3 presents the calibrated water retention curve, which is similar to the wetting curves of Opalinus clay measured in other studies [144]. Tables 1 and 2 present the calibrated mechanical and hydraulic parameters for Opalinus clay, respectively.

The evolution of water content and anisotropic strains are presented in Figure 4. We observe a close match between the experimental data and the model prediction of the water content evolution between days 0–10 and days 21–29. When a suction of 39.0 MPa was applied between days 10–21, the model predicted a slower rate of water content increase. On the other hand, the model predicted a quicker equilibration of the sample with the applied suction of 9.8 MPa compared to the experimental data during days 29–40. Similarly, the trend of strain evolution during days 0–21 follows that of the experimental data, but the model overestimates the rate of swelling when lower suctions are

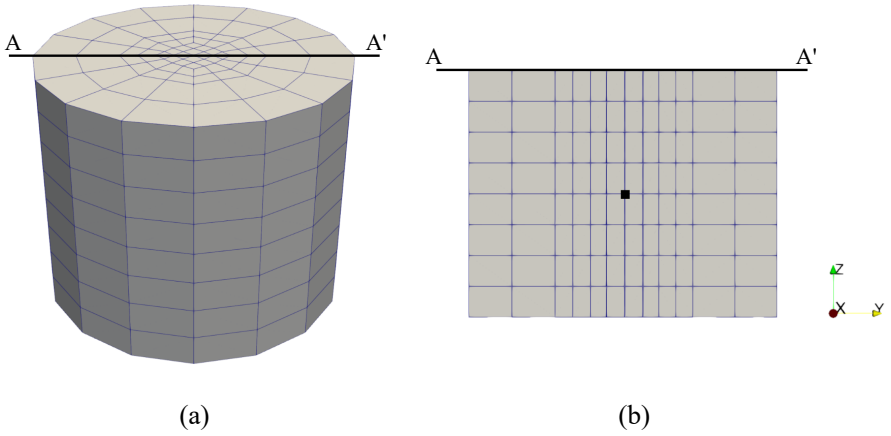

Fig. 2. (a) 3D mesh of cylindrical sample (20 mm tall, 25 mm diameter) and (b) cross-section of the mesh on the y-z plane.

applied. This may indicate the inadequacy of the van Genuchten-Mualem relative permeability equation in capturing the unsaturated hydraulic behavior of clayey rocks [2]. Instead, a homogenization scheme for the relative permeability may need to be developed for the microstructure of clayey rocks [11]. This is outside the scope of the current study and will be investigated in a future work.

The predicted anisotropic strains at equilibrium shown in Figure 4 are a good match to the experimental data between days 0–29. However, the model underestimates the anisotropic strains at 9.8 MPa. This can be attributed to

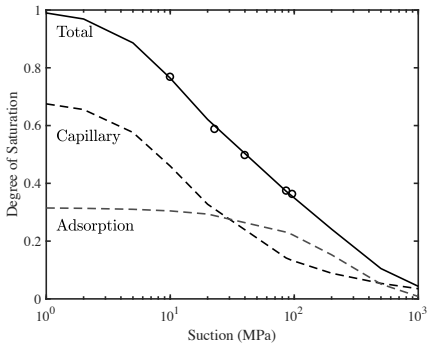

Fig. 3. Adsorbed, capillary, and total water retention curves for Opalinus clay. Ticks are data points from Minardi et al. [100].

Table 1. Mechanical constitutive parameters for Opalinus clay used in swelling tests [50, 80, 126, 136, 142]. Porosities listed correspond to the sample's initial condition.

Parameter	Value
Nanoscale	
SSA (m^2/g)	85
n (mol/m)	100
ϕ^m	0.13
μ (GPa)	3
Microscale	
MPD	4
ξ	0.35
ϕ^μ	0.31
Macroscale	
ϕ^{quartz}	0.32
ϕ^{calcite}	0.21
K^{quartz} (GPa)	38
μ^{quartz} (GPa)	44
K^{calcite} (GPa)	70
μ^{calcite} (GPa)	32
ξ^i	0.8

Table 2. Hydraulic parameters for Opalinus clay used in swelling tests [50, 80, 136, 142].

Parameter	Value
Water retention curve	
θ_{sat}	0.19
$\theta_a^{\max}$	0.06
α (MPa)	7.0
n	1.67
m_{ads}	1
Permeabilities	
κ_m (m^2)	$1.0\text{x}10^{-23}$
$\kappa_{M,\perp}$ (m^2)	$1.0\text{x}10^{-20}$
$\kappa_{M,\parallel}$ (m^2)	$2.0\text{x}10^{-20}$
$\bar{\alpha}$ (m^{-2})	20.0
$\bar{k}$ (m^2)	$1.0\text{x}10^{-23}$

the proposed model neglecting plastic behavior, which shales including Opalinus clay are known to exhibit when undergoing drying and wetting processes [119, 163, 165]. The BN and BP strains were underestimated by 0.18% and 0.13%, respectively. We compare this against the plastic deformation that the sample exhibited. After the free swelling test, Minardi et al. [100] subjected the sample to a drying test with the same applied suctions. By comparing the anisotropic strains after the cyclic free swelling/drying test, we can determine the plastic strains normal to and along the bedding plane. At an applied

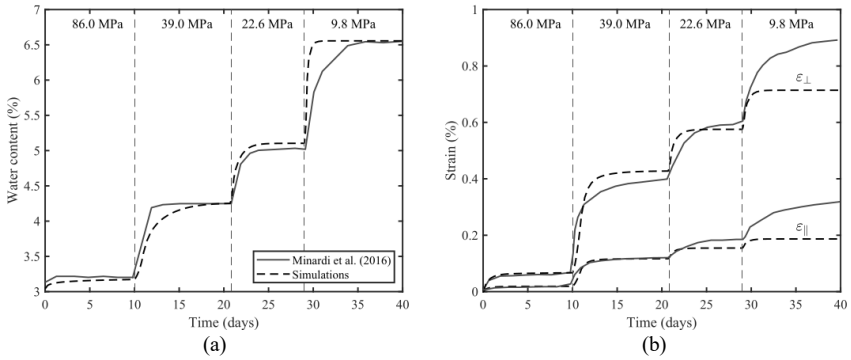

Fig. 4. Time evolution of (a) water content and (b) strains during free swelling test of Opalinus clay. Solid curves are experimental data from Minardi et al. [100]; dashed curves are model predictions

suction of 86.0 MPa, the sample underwent permanent strains of 0.18% and 0.03% in the BN and BP directions, respectively. Thus, the difference in strains between the model predictions and the experimental data at lower suctions is mostly a result of neglecting plastic deformations, which will be explored in a future study.

5.2 Poroelastic coefficients

In this section, we elucidate the impact of the derived double-porosity formulation on the poroelastic coefficients and their evolution with the degree of saturation. Figure 5 presents the evolution of the stiffness moduli and Poisson's ratios with saturation for the Opalinus clay samples calibrated from free swelling tests. We note the strong similarities between the evolution of the stiffness moduli for the calibrated Opalinus clay sample and the experimental stiffness moduli data presented in Yurikov et al. [151]. The BP stiffness moduli are more sensitive to the degree of saturation and decrease more significantly upon saturation of the sample as compared to the out-of-plane stiffness moduli, which remain approximately constant. This behavior has also been observed in various shales [71, 133, 153, 162].

On the other hand, measurements of Poisson's ratios presented in the literature differ from our model's predictions. The model predicts decreasing Poisson's ratios in both the BN and BP directions as the sample saturates. However, experimental data of anisotropic shales have generally shown the Poisson's ratios to increase with the degree of saturation [133, 151, 162]. This may indicate the presence of microstructural features in shale that influence its elastic properties, especially the Poisson's ratio, but are not yet accounted for in the proposed model.

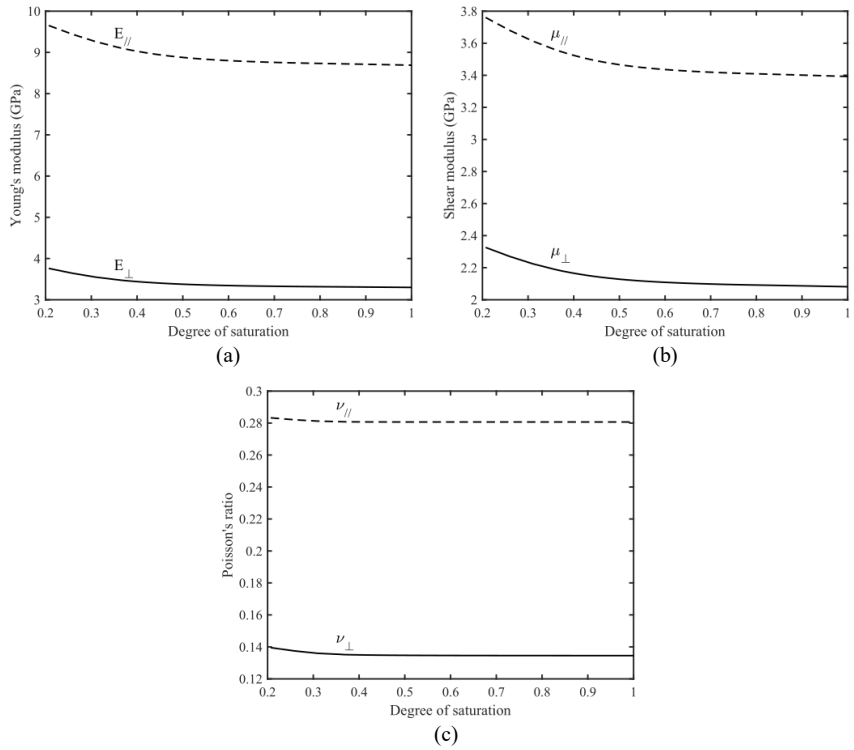

Fig. 5. Variation of (a) Young's moduli, (b) shear moduli, and (c) Poisson's ratios with degree of saturation for Opalinus clay calibrated against data from Minardi et al. [100].

Figure 6(a) presents the evolution of the BN and BP components of the Biot tensors. The components of the nanopore and micropore Biot tensors generally remain constant with saturation. The micropore Biot tensor components are slightly larger when the sample is drier, which can be attributed to the decrease in micropore porosity as the sample saturates, a characteristic of the water retention curve adopted in this study. Simultaneously, the nanopore porosity increases during a wetting process and results in a slight increase in the nanopore Biot tensor components. The nanopore Biot tensor components are also significantly smaller than those of the micropore Biot tensor, as the nanopores are much stiffer due to the high aspect ratio of their geometry. Overall, the Biot tensor components are within the range of experimental measurements for most shales [12, 64, 65, 140].

The storage coefficients, $\mathcal{C}_M$ and $\mathcal{C}_m$ are presented in Figures 6(b) and 6(c). The storage coefficients generally increase upon saturation of the sample, which reflects an increase in pore space as the sample swells. We note that the predicted values are much smaller than the measured storage coefficient

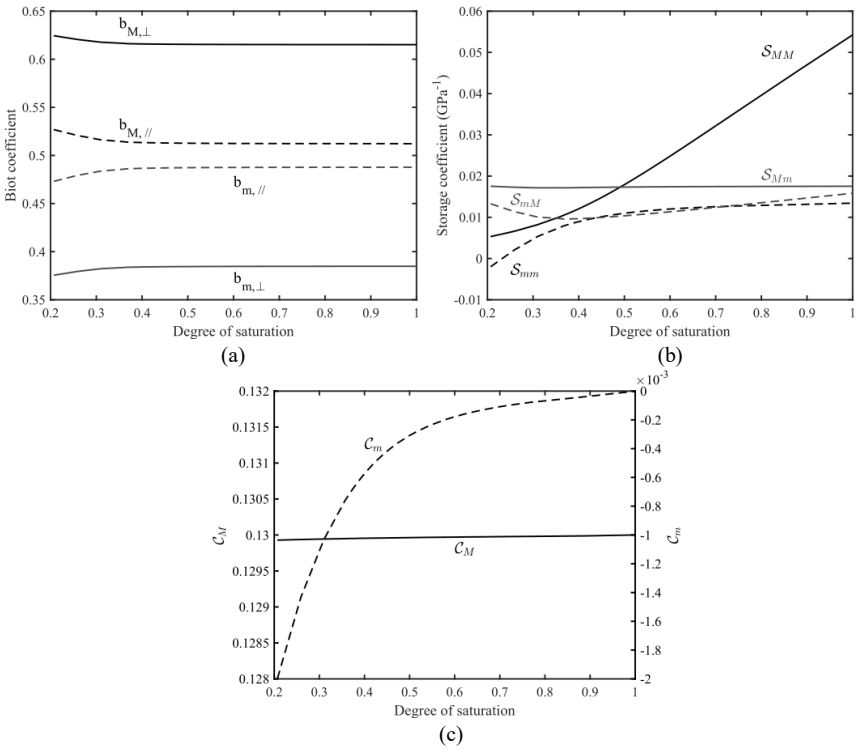

Fig. 6. Variation of (a) Biot tensor components, (b) storage coefficients, (c) $\mathcal{C}_M$ and $\mathcal{C}_m$ with degree of saturation for Opalinus clay calibrated against data from Minardi et al. [100].

of most shales [12, 103]. Separately, $\mathcal{C}_M$ stays relatively constant as saturation increases, while $\mathcal{C}_m$ increases upon wetting of the sample and is also negative for all degrees of saturation.

We also investigate the variation of the surface tension terms with the degree of saturation, as presented in Figure 7. The components of the surface tension coefficient, $\boldsymbol{b}_\omega$, decrease with saturation of the sample. We note that the surface tension term p^{eq} is small compared to the pore pressures and stresses in the sample: it is on the order of kPa between 20% and 100% saturation. As such, the surface tension term can be considered as negligible when simulating the Opalinus clay sample.

Lastly, we also investigate the evolution of the nanopore permeability tensor components with the degree of saturation presented in Figure 8. The nanopore permeability tensor components, which depend on the interlayer spacing, h, increase with saturation. The BP component has a larger increase. Overall, the nanopore permeability anisotropy remains approximately con-

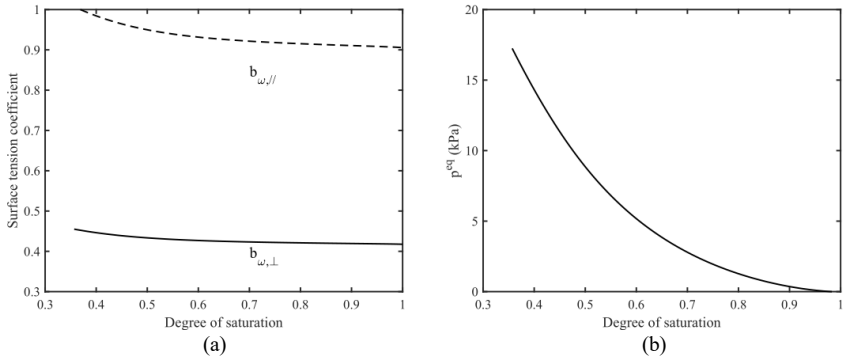

Fig. 7. Variation of (a) surface tension coefficient $\boldsymbol{b}_\omega$ components and (b) p^{eq} with degree of saturation for Opalinus clay calibrated against data from Minardi et al. [100].

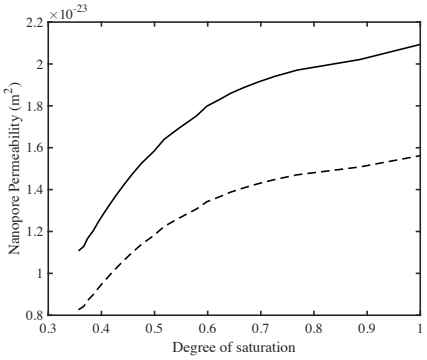

Fig. 8. Variation of nanopore permeability with degree of saturation for Opalinus clay calibrated against data from Minardi et al. [100].

stant ($\kappa_{m,\parallel}/\kappa_{m,\perp} = 1.34$) since the MPD does not vary with the degree of saturation.

5.3 Constant volume swelling test

Next, we elucidate the effects of the proposed double-porosity formulation on the swelling behavior of Opalinus clay under isochoric conditions. We first validate the model parameters against constant volume swelling test measurements from Crisci [36]. Then, we simulate constant volume swelling tests to determine the evolution of swelling pressures in Opalinus clay.

Volumetric strain evolution

Crisci [36] conducted a swelling test under isochoric conditions, in which the sample is placed in contact with water and prevented from swelling by progressively increasing the radial and vertical stresses. The cylindrical (77 mm tall, 38 mm diameter) sample was cored perpendicular to the bedding planes and had an initial void ratio and saturation of 0.14 and 78%, respectively. The sample was placed in contact with water and the axial and radial stresses were increased so as to prevent swelling of the sample. Crisci [36] presented the axial and radial stresses applied as well as the volumetric strains of the sample during the saturation process.

Following the testing procedure in Crisci [36], we simulated the same axial and radial stresses on an Opalinus clay sample and validated our results against the volumetric strain measurements. The suction in the sample is assumed to be initially 9 MPa. Nanopore and micropore water pressures of 1 MPa are then applied on the top and bottom surfaces. We adopt the same mechanical parameters (excluding the porosity values) calibrated in the previous section (Table 1). Table 3 presents the hydraulic parameters assumed for the Opalinus clay sample tested in Crisci [36].

Table 3. Hydraulic parameters for Opalinus clay used in constant volume swelling tests [36, 50, 80, 136, 142].

Parameter	Value
Water retention curve	
θ_{sat}	0.12
$\theta_a^{\max}$	0.04
α (MPa)	7.0
n	1.67
m_{ads}	1
Permeabilities	
κ_m (m^2)	$1.0\text{x}10^{-22}$
$\kappa_{M,\perp}$ (m^2)	$1.0\text{x}10^{-20}$
$\kappa_{M,\parallel}$ (m^2)	$2.0\text{x}10^{-20}$
$\bar{\alpha}$ (m^{-2})	20.0
$\bar{k}$ (m^2)	$1.0\text{x}10^{-22}$

Figure 9a presents the axial and radial stresses applied to the Opalinus clay sample during the constant volume swelling test. Crisci noted that the sample tended to swell first in the bedding normal direction and thus, the higher axial stresses were applied to compensate for the swelling of the sample. The volumetric strains the develop in the sample during saturation are presented in Figure 9b. We note that the sample develops small volumetric strains of around 0.06%, on the order of 10^{-4} (or 10^{-2}%). The predicted final volumetric strain after 12 days is close to the experimental measurements

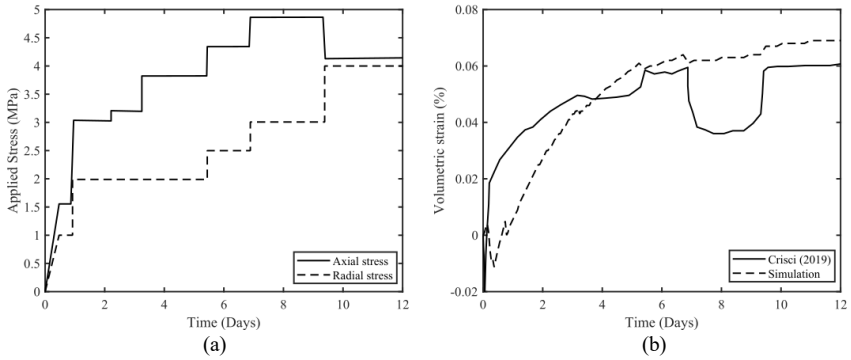

Fig. 9. Time evolution of (a) axial and radial stresses applied on the sample and (b) volumetric strains for an Opalinus clay sample during constant volume swelling test. Positive volumetric strains indicate expansion of the sample.

from the constant volume swelling test. The initial slope of volumetric strain in our simulation is gentler than the measured volumetric strain evolution. This likely further highlights that the relative permeability equation used in our model is inadequate for modeling unsaturated fluid flow in clayey rocks. The tested sample also undergoes notable volumetric contraction when the applied stresses were further increased around day 9, which our simulations are unable to fully capture. This may be due to plastic strains developing in the sample at higher applied stresses and possibly loading collapse as the sample becomes more saturated. Still, considering that the Opalinus clay sample was taken from a different depth than the sample tested in Minardi et al [100], we believe that the mechanical parameters are generally well calibrated for Opalinus clay samples.

Swelling pressures

The swelling pressures of clayey rocks are of interest in many applications of these rocks. To elucidate the evolution of swelling pressures, we simulate another constant volume swelling test of Opalinus clay. The sample is confined both axially and laterally with Dirichlet boundary conditions on the top and radial surfaces, such that its volume is kept constant throughout the swelling test. The sample is initially at 90% saturation, which corresponds to an initial suction of 4.5 MPa. Nanopore and micropore water pressures of 0 MPa are applied on the bottom surface [139]. The pore water pressures on the bottom surface are applied over approximately one hour, and their variation over time is presented in Figure 10a.

Figure 10b presents the axial and radial swelling pressures that develop in the sample during the swelling test. The axial pressures that develop are higher than the radial pressures, similar to observations of swelling pressures in clays

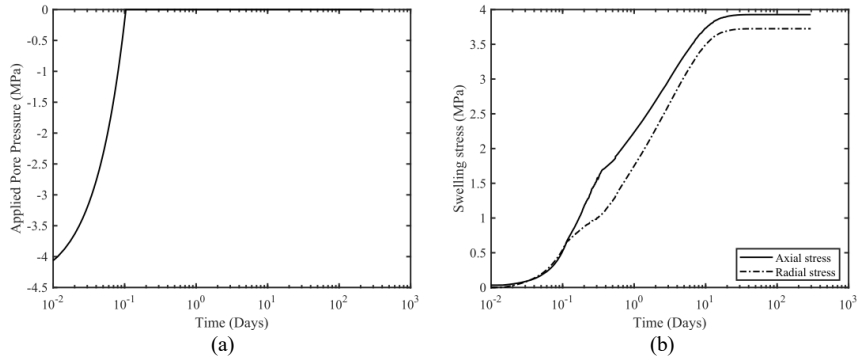

Fig. 10. Time evolution of (a) nanopore and micropore water pressures applied on the bottom surface of the sample and (b) axial and radial swelling pressures for an Opalinus clay sample during constant volume swelling test.

[6, 77, 118], and can be attributed to structural anisotropy of the Opalinus clay fabric. After the 0 MPa pore pressures are applied, the axial pressures increase steadily until a maximum axial swelling pressure of 3.8 MPa. The maximum swelling pressure is close to the experimental data reported in Favero et al. [49] of 3.0 MPa and 3.7 MPa for two different samples of Opalinus clay.

On the other hand, the radial pressures first increase gently until around 7 hours, before increasing at a faster rate to a maximum swelling pressure of 3.6 MPa. We attribute this behavior to the evolution of pore pressures in the sample, which are presented in Figure 11 at the nodal point represented by the black square in Figure 2(b). The micropore pressure remains constant at -4.5 MPa during the application of 0 MPa pore pressures on the sample, then steadily increases to 0 MPa within approximately 7 hours. In comparison, the nanopore pressure first decreases to around -7 MPa, before increasing to 0 MPa. The time when the nanopore pressures decrease corresponds to the change in the slope of the radial swelling pressure curve, and is a result of the micropores saturating first due to their higher permeability. The micropores expand which reduces the nanopore porosity and causes the nanopore pressure to decrease as prescribed by the water retention curve adopted in our model. Over time, fluid flows into the nanopores and their volume increases as they saturate, thus increasing the nanopore pressure.

To investigate the effect of using a double-porosity framework, we compare the swelling pressures against that of a sample of a single-porosity material. For the single-porosity material, we set the nanopore permeability to 0 m^2 and the interface permeability to $4.0\text{x}10^{-15}$ m^2, such that the micropore and nanopore pressures equilibrate almost instantly. All other material properties are kept constant so that the mechanical properties of both samples are the same. Figure 12 compares the axial and radial swelling pressures that develop in samples of the two materials during a constant volume swelling test.

While both samples attain the same maximum swelling pressures, the trend of swelling pressure evolution differs significantly between the single-porosity and double-porosity samples. As expected, the single-porosity sample saturates at a much faster rate than the double-porosity sample and reaches the maximum swelling pressure within around 8 hours from the start of the test. Furthermore, the rate of swelling is constant in the single-porosity sample throughout the test, unlike the double-porosity sample where there is a change in the rate of swelling due to differences in the micropore and nanopore pressures.

Uniaxial swelling tests

We also consider uniaxial swelling tests, in which the sample is prevented from swelling in the axial direction but is free to swell laterally. A Dirichlet boundary condition is applied on the top surface to prevent any axial displacement. Pore water pressures of 0 MPa are once again applied on the bottom surface of the sample.

The axial swelling pressure evolution is presented in Figure 13 for different bedding plane orientations. The development of swelling pressure is similar to that of the constant volume swelling test. It increases after 0 MPa pore pressures are applied until a maximum swelling pressure over a period of approximately 30 days. The sample with $\theta = 90°$ has the highest maximum swelling pressure of around 2.6 MPa, while the sample with $\theta = 0°$ only develops 1.0 MPa of maximum swelling pressure. Additionally, the maximum swelling pressure does not vary linearly with the bedding plane orientation as the sample with $\theta = 45°$ attains a maximum swelling pressure 2.2 MPa. We note that the maximum swelling pressures obtained from uniaxial swelling test simulations are smaller, but within the same magnitude, than those presented by Zhang et al. [152] for an Opalinus clay sample.

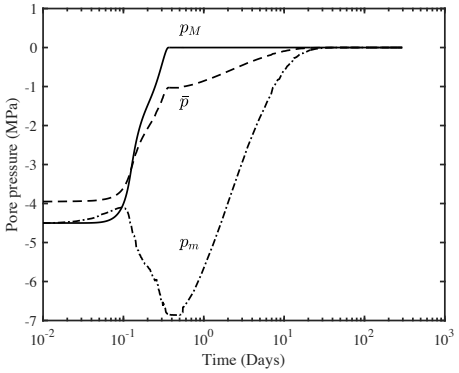

Fig. 11. Evolution of nanopore and micropore pressures in an Opalinus clay sample during constant volume swelling test.

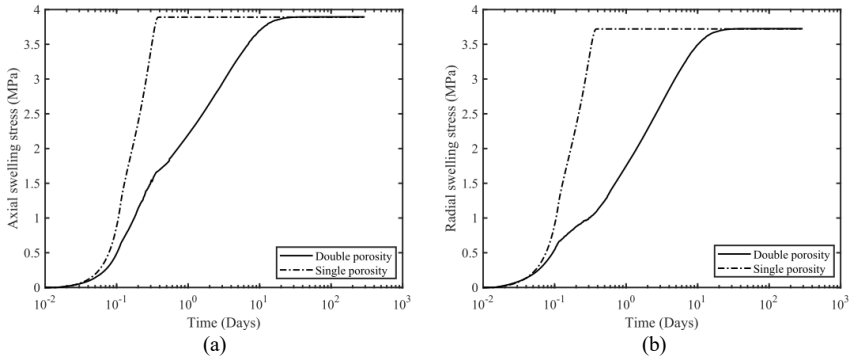

Fig. 12. Comparison of (a) axial and (b) radial swelling pressures between single-porosity and double-porosity samples of Opalinus clay during constant volume swelling tests.

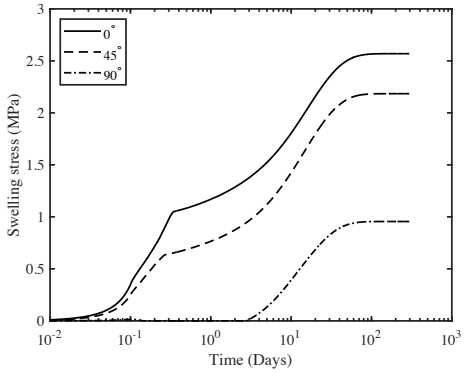

Fig. 13. Evolution of axial swelling pressures for Opalinus clay samples with different bedding plane orientations, θ, during uniaxial swelling tests.

We also investigate the predicted pore pressure distributions in the sample with $\theta = 45°$. Figures 14 and 15 present the pore pressure distributions at different times in the uniaxial swelling test in the micropores and nanopores, respectively. We observe the effect of the bedding plane orientation on the pore pressure distributions in both the micropore and nanopore pressures. Since the permeability along the bedding plane is larger, the left end of the sample saturates faster. The effect of the bedding plane orientation is more noticeable for the micropore pressure distribution, which is a result of higher permeability anisotropy in the micropores (Figure 8). The micropores also have a higher permeability than the nanopores, and thus saturate within a few hours. In comparison, the nanopores take nearly 20 days to saturate.

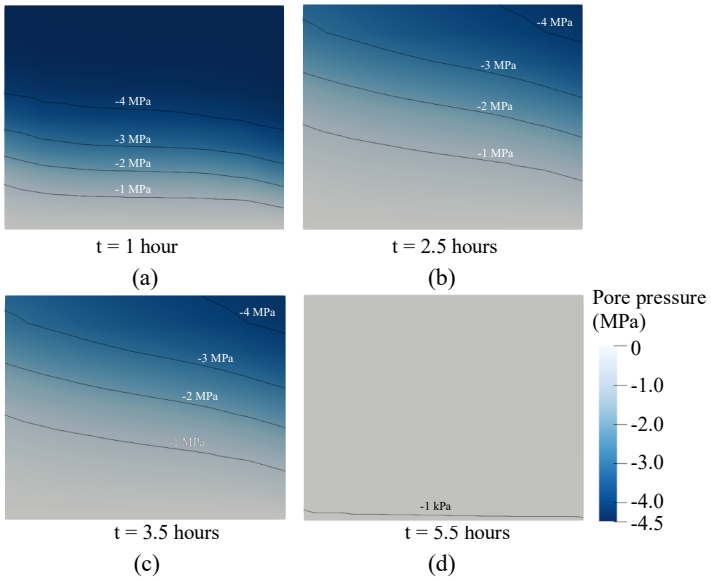

Fig. 14. Time evolution of micropore pressure distributions for a cross-section of an Opalinus clay sample with 45° bedding plane orientation during uniaxial swelling test: (a) 1 hour, (b) 2.5 hours, (c) 3.5 hours and (d) 5.5 hours.

6 Conclusion

In this study, we have presented a double porosity framework for coupled unsaturated fluid flow and solid deformation in anisotropic clayey rocks. The governing equations were derived based on a three-level homogenization scheme by upscaling the microscopic strains and porosity evolutions. The homogenization scheme, and by extension, the proposed framework, accounts for the microstructure of clay rocks at the nano, micro, and macroscales. Numerical simulations of free swelling behavior in Opalinus clay were conducted with a three-field mixed finite element formulation. Results demonstrate the proposed framework's ability to capture the time evolution of water content and anisotropic strain in Opalinus clay. Simulations of confined swelling tests were also conducted for Opalinus clay and the predicted swelling pressures match closely to experimental data.

The results of this study highlight the need to incorporate the effects of microstructure on macroscopic mechanical and hydraulic properties when simulating multiscale materials such as clayey rocks. The macroscopic elastic parameters can evolve with the degree of saturation, a property which is rarely accounted for in many unsaturated hydromechanical frameworks. Furthermore, the effect of multiple porosities should be considered when modeling clayey rocks. Our results show that the interaction between pores at

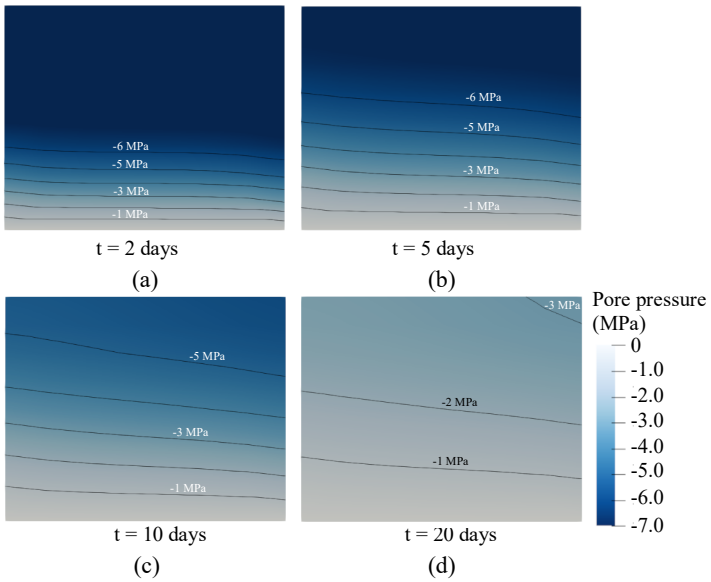

Fig. 15. Time evolution of nanopore pressure distributions for a cross-section of an Opalinus clay sample with 45° bedding plane orientation during uniaxial swelling test: (a) 2 days, (b) 5 days, (c) 10 days and (d) 20 days.

multiple scales can impact the macroscopic development of pore pressures and swelling pressures in these rocks. A single porosity framework lacks the ability to capture this interaction. Further work is underway to incorporate plasticity [20, 73, 123, 163, 164], viscoplasticity [22, 90, 91], chemical-induced transport [23, 66], and geometric nonlinearity [128, 129] in the homogenization scheme, as well as a homogenization scheme that upscales the micropore permeability accounting for the microstructure in clayey rocks.

Appendix A. Eigenstrain influence tensor

The expressions of the eigenstrain influence tensor $\bar{\mathbb{B}}$ are presented below [116]. For the general case where each phase of the composite material is associated with a different Hill's tensor, $\bar{\mathbb{B}}$ can be written as

$$\begin{aligned}\bar{\mathbb{B}}^{\alpha\alpha} =& \left(\mathbb{I} - \phi^{\alpha}\mathbb{A}^{\alpha}\right) : \bar{\mathbb{A}}^{\alpha} : \mathbb{P}^{\alpha} + \phi^{\alpha}\left(\mathbb{A}^{\alpha} : \overline{\bar{\mathbb{A}} : \mathbb{P}}) - \bar{\mathbb{A}}^{\alpha} : \mathbb{P}^{\alpha}\right) : \\ & Q : \left((\mathbb{C}^{\text{hom}} - \mathbb{C}^{\alpha}) : \bar{\mathbb{A}}^{\alpha} : \mathbb{P}^{\alpha} + \mathbb{I} - \mathbb{A}^{\alpha}\right) \\ \bar{\mathbb{B}}^{\alpha\beta} =& -\phi^{\beta}\mathbb{A}^{\alpha} : \bar{\mathbb{A}}^{\beta} : \mathbb{P}^{\beta} + \phi^{\beta}\left(\mathbb{A}^{\alpha} : \overline{\bar{\mathbb{A}} : \mathbb{P}} - \bar{\mathbb{A}}^{\alpha} : \mathbb{P}^{\alpha}\right) : \\ & Q : \left((\mathbb{C}^{\text{hom}} - \mathbb{C}^{\beta}) : \bar{\mathbb{A}}^{\beta} : \mathbb{P}^{\beta} + \mathbb{I} - \mathbb{A}^{\beta}\right)\end{aligned} \tag{71}$$

where

$$\begin{aligned} Q &= \overline{(\mathbb{C}^{\text{hom}} - \mathbb{C}^{\gamma}) : \bar{\mathbb{A}}^{\gamma} : \mathbb{P}^{\gamma}}^{-1} \\ \bar{\mathbb{A}}^{\gamma} &= (\mathbb{I} + \mathbb{P}^{\gamma} : (\mathbb{C}^{\gamma} - \mathbb{C}^{\text{matrix}}))^{-1} \end{aligned} \tag{72}$$

and N^p is the number of phases in the composite material.

This can be simplified for a two-phase material, regardless of microstructural geometry and phase properties, to

$$\begin{aligned} \bar{\mathbb{B}}^{\alpha\alpha} &= \left(\mathbb{I} - \phi^{\alpha}\mathbb{A}^{\alpha}\right) : \bar{\mathbb{A}}^{\alpha} : \mathbb{P} \\ \bar{\mathbb{B}}^{\alpha\beta} &= -\phi^{\beta}\mathbb{A}^{\alpha} : \bar{\mathbb{A}}^{\beta} : \mathbb{P} \end{aligned} \tag{73}$$

Appendix B. Poroelastic coefficients

$$\mathcal{C}_m = \frac{\phi^m}{\phi^n}(\phi^{\mu} p_M \mathbf{1} : {}^{\mu}\mathbb{A}^m : {}^{m}\bar{\mathbb{B}}^{mm} : {}^{\mu}\mathbb{A}^{p\mathsf{T}} : \mathbf{1} + p_M \mathbf{1} : {}^{\mu}\bar{\mathbb{B}}^{mp} : \mathbf{1}) \tag{74a}$$

$$\tilde{\mathcal{C}}_M = \phi^M(\phi^{\mu} p_M \mathbf{1} : {}^{\mu}\mathbb{A}^p : {}^{m}\bar{\mathbb{B}}^{mm} : {}^{\mu}\mathbb{A}^{p\mathsf{T}} : \mathbf{1} + p_M \mathbf{1} : {}^{\mu}\bar{\mathbb{B}}^{pp} : \mathbf{1}) \tag{74b}$$

$$\tilde{\mathcal{S}}_{MM} = \phi^M(S^w \phi^{\mu} \mathbf{1} : {}^{\mu}\mathbb{A}^p : {}^{m}\bar{\mathbb{B}}^{mm} : {}^{\mu}\mathbb{A}^{p\mathsf{T}} : \mathbf{1} + S^w \mathbf{1} : {}^{\mu}\bar{\mathbb{B}}^{pp} : \mathbf{1}) \tag{74c}$$

$$\mathcal{S}_{mM} = \frac{\phi^m}{\phi^n}(\phi^{\mu} S^w \mathbf{1} : {}^{\mu}\mathbb{A}^m : {}^{m}\bar{\mathbb{B}}^{mm} : {}^{\mu}\mathbb{A}^{p\mathsf{T}} : \mathbf{1} + S^w \mathbf{1} : {}^{\mu}\bar{\mathbb{B}}^{mp} : \mathbf{1}) \tag{74d}$$

$$\boldsymbol{\mathcal{S}}_{mm} = \frac{\phi^m}{\phi^n}((1-\phi^{\mu})\mathbf{1} : {}^{\mu}\mathbb{A}^m : {}^{m}\bar{\mathbb{B}}^{mm} : {}^{\mu}\mathbb{A}^{m\mathsf{T}} + \mathbf{1} : {}^{\mu}\bar{\mathbb{B}}^{mm}) \tag{74e}$$

$$\boldsymbol{\mathcal{S}}_{Mm} = \phi^M((1-\phi^{\mu})\mathbf{1} : {}^{\mu}\mathbb{A}^p : {}^{m}\bar{\mathbb{B}}^{mm} : {}^{\mu}\mathbb{A}^{m\mathsf{T}} + \mathbf{1} : {}^{\mu}\bar{\mathbb{B}}^{pm}) \tag{74f}$$

Appendix C. Finite element formulation

We formulate a three-field $\boldsymbol{u}/p_M/p_m$ mixed finite element solution that accommodates for multiscale effects in an unsaturated double porosity medium. We assume that the ion concentration, π, is constant with time and thus all $\dot{\pi}$-terms drop out of the governing equations. Equal-order interpolation is adopted for the displacement and pressure fields to reduce the size of the matrix problem, but with a stabilization feature that ensures satisfaction of the weak inf-sup condition [32]. The mixed-finite element formulation is implemented in Geocentric, a massively parallel finite element code for geomechanics [143] built on the deal.II finite element library [3, 8], p4est mesh handling library [24], and the Trilinos project [67].

To develop the finite element formulation, we first express the three-field conservation laws equations (7), (59), and (60) as volume integrals in variational form with the relevant initial and boundary conditions. Consider a

problem domain $\mathcal{B}$ with external boundary $\partial\mathcal{B}$. The boundary can be decomposed into non-overlapping essential and natural boundaries on which the following conditions must be satisfied:

Solid deformation:

$$\left.\begin{aligned} \boldsymbol{u} &= \bar{\boldsymbol{u}} \quad \text{on} \quad \partial\mathcal{B}_u \\ \boldsymbol{n}\cdot\boldsymbol{\sigma} &= \bar{\boldsymbol{t}} \quad \text{on} \quad \partial\mathcal{B}_t \end{aligned}\right\}, \tag{75}$$

where $\bar{\boldsymbol{u}}$ is the prescribed value of displacement field $\boldsymbol{u}$ on the boundary $\partial\mathcal{B}_u$, and $\boldsymbol{n}$ is the outward unit normal vector to the boundary $\partial\mathcal{B}_t$ on which the surface traction $\bar{\boldsymbol{t}}$ is prescribed.

Fluid flow in the nanopores/micropores:

$$\left.\begin{aligned} p_\alpha &= \hat{p}_\alpha \quad \text{on} \quad \partial\mathcal{B}_{p\alpha} \\ -\boldsymbol{n}_\alpha\cdot\boldsymbol{q}_\alpha &= \hat{q}_\alpha \quad \text{on} \quad \partial\mathcal{B}_{q\alpha} \end{aligned}\right\}, \tag{76}$$

where $\alpha = m, M$ for the nanopores and micropores, respectively, $\boldsymbol{n}_\alpha$ is the outward unit normal vector to the boundary $\partial\mathcal{B}_{q\alpha}$ on which the normal fluid flux $\hat{q}_\alpha$ is prescribed, and $\hat{p}_\alpha$ is the prescribed value of the pore pressure p_α on the boundary $\partial\mathcal{B}_{p\alpha}$.

The variational equation for the balance of linear momentum then takes the form

$$\begin{aligned} &\int_{\mathcal{B}} \nabla^s\boldsymbol{\eta} : (\boldsymbol{\sigma}' - S^w p_M \boldsymbol{b}_M - p_m \boldsymbol{b}_m - \pi \boldsymbol{b}_\pi + p^{eq}\boldsymbol{b}_\omega)\,\mathrm{d}V \\ &\qquad = \int_{\mathcal{B}} \boldsymbol{\eta}\cdot(\rho\boldsymbol{g} - \bar{\boldsymbol{c}})\,\mathrm{d}V + \int_{\partial\mathcal{B}_t} \boldsymbol{\eta}\cdot\bar{\boldsymbol{t}}\,\mathrm{d}A\,, \end{aligned} \tag{77}$$

where $\boldsymbol{\eta}$ is the weighting function for displacement and $\nabla^s = (\nabla + \nabla^{\mathsf{T}})/2$ is the symmetric gradient operator

The balance of mass for fluid in the micropores in variational form reads

$$\begin{aligned} &\int_{\mathcal{B}} \varphi S^w \boldsymbol{b}_M : \nabla^s\boldsymbol{v}\,\mathrm{d}V + \int_{\mathcal{B}} \varphi\Big(\mathcal{C}_M\dot{S}^w + \mathcal{S}_{MM}\dot{p}_M + \mathcal{S}_{Mm}\dot{p}_m\Big)\,\mathrm{d}V \\ &\quad + \int_{\mathcal{B}} \varphi\frac{1}{K_w}\nabla p_M\cdot\boldsymbol{q}_{wM}\,\mathrm{d}V - \int_{\mathcal{B}} \nabla\varphi\cdot\boldsymbol{q}_{wM}\,\mathrm{d}V \\ &\quad - \int_{\mathcal{B}} \varphi\frac{c_{wM}}{\rho_w}\,\mathrm{d}V = \int_{\partial\mathcal{B}_{qM}} \varphi\hat{q}_M\,\mathrm{d}A\,, \end{aligned} \tag{78}$$

where $\boldsymbol{v} = \dot{\boldsymbol{u}}$ and φ is the weighting function for the pore water pressure in the micropores.

For the nanopores, the balance of mass variational equation is

$$\int_{\mathcal{B}} \xi \boldsymbol{b}_m : \nabla^s \boldsymbol{v} \, \mathrm{d}V + \int_{\mathcal{B}} \xi \Big(\mathcal{C}_m \dot{S}^w + \mathcal{S}_{mM} \dot{p}_M + \mathcal{S}_{mm} \dot{p}_m \Big) \, \mathrm{d}V + \int_{\mathcal{B}} \xi \frac{1}{K_w} \nabla p_m \cdot \boldsymbol{q}_{wm} \, \mathrm{d}V - \int_{\mathcal{B}} \nabla \xi \cdot \boldsymbol{q}_{wm} \, \mathrm{d}V - \int_{\mathcal{B}} \xi \frac{c_{wm}}{\rho_w} \, \mathrm{d}V = \int_{\partial \mathcal{B}_{q_m}} \xi \hat{q}_m \, \mathrm{d}A \,, \tag{79}$$

where ξ is the weighting function for the pore water pressure in the nanopores.

We adopt the unconditionally stable and first-order accurate backward difference scheme to perform time integration of the variational equations. For the unsaturated micropores, we first insert the water retention law to express $\dot{S}^w$ in terms of $\dot{p}_M$, then time-integrate the pressure. Then, Equation (78) after time integration can be rewritten as

$$\int_{\mathcal{B}} \varphi S^w \boldsymbol{b}_M : (\nabla^s \boldsymbol{u} - \nabla^s \boldsymbol{u}_n) \, \mathrm{d}V + \int_{\mathcal{B}} \varphi \bar{\mathcal{S}}_M (p_M - p_{M,n}) \, \mathrm{d}V + \int_{\mathcal{B}} \varphi \mathcal{S}_{Mm} (p_m - p_{m,n}) \, \mathrm{d}V - \Delta t \int_{\mathcal{B}} \boldsymbol{f}_M \cdot \boldsymbol{q}_{wM} \, \mathrm{d}V - \Delta t \int_{\mathcal{B}} \varphi \frac{c_{wM}}{\rho_w} \, \mathrm{d}V = \Delta t \int_{\partial \mathcal{B}_{q_M}} \varphi \hat{q}_M \, \mathrm{d}A \,, \tag{80}$$

where $\bar{\mathcal{S}}_M$ is defined as

$$\bar{\mathcal{S}}_M = \mathcal{S}_{MM} + \mathcal{C}_M \frac{\partial S^w}{\partial p_M} \,, \tag{81}$$

$$\boldsymbol{f}_M(\varphi, \nabla \varphi) = \nabla \varphi - \varphi \frac{1}{K_w} \nabla p_M \,. \tag{82}$$

and $\Delta t = t_{n+1} - t_n$ is the time increment, with subscript n indicating that the variable is evaluated at time t_n.

For the nanopores, we have

$$\int_{\mathcal{B}} \xi \psi^m \boldsymbol{b}_m : (\nabla^s \boldsymbol{u} - \nabla^s \boldsymbol{u}_n) \, \mathrm{d}V + \int_{\mathcal{B}} \xi \bar{\mathcal{S}}_m (p_M - p_{M,n}) \, \mathrm{d}V + \int_{\mathcal{B}} \xi \mathcal{S}_{mm} (p_m - p_{m,n}) \, \mathrm{d}V - \Delta t \int_{\mathcal{B}} \boldsymbol{f}_m \cdot \boldsymbol{q}_{wm} \, \mathrm{d}V - \Delta t \int_{\mathcal{B}} \xi \frac{c_{wm}}{\rho_w} \, \mathrm{d}V = \Delta t \int_{\partial \mathcal{B}_{q_m}} \xi \hat{q}_m \, \mathrm{d}A \,, \tag{83}$$

where

$$\bar{\mathcal{S}}_m = \mathcal{S}_{mM} + \mathcal{C}_m \frac{\partial S^w}{\partial p_M} \,, \tag{84}$$

$$\boldsymbol{f}_m(\xi, \nabla\xi) = \nabla\xi - \xi\frac{\nabla p_m}{K_w}\,. \tag{85}$$

Next, we write the finite element vector equations in residual form by substituting the matrix approximations of the weighting functions $\boldsymbol{\eta}$, φ, ξ and their derivatives, into the time-integrated variational equations. For the balance of linear momentum (77), we write

$$\begin{aligned}\boldsymbol{\mathcal{R}}_u = &\int_{\mathcal{B}} \boldsymbol{B}^{\mathsf{T}}\{\boldsymbol{\sigma}' - S^w p_M^h \boldsymbol{b}_M - p_m^h \boldsymbol{b}_m - \pi^h \boldsymbol{b}_\pi + p^{eq}\boldsymbol{b}_\omega\}\,\mathrm{d}V \\ &- \int_{\mathcal{B}} \boldsymbol{N}^{\mathsf{T}}(\rho\boldsymbol{g} - \bar{\boldsymbol{c}})\,\mathrm{d}V - \int_{\partial\mathcal{B}_t} \boldsymbol{N}^{\mathsf{T}}\bar{\boldsymbol{t}}\,\mathrm{d}A\,,\end{aligned} \tag{86}$$

where $\boldsymbol{N}$ is the displacement shape function matrix, $\boldsymbol{B}$ is the strain-displacement matrix, and superscript h in the pressure term indicates a Galerkin approximation. The braces $\{\cdot\}$ indicate that the stress terms inside are written in Voigt notation.

For the balance of fluid mass in the micropores, we have

$$\begin{aligned}\boldsymbol{\mathcal{R}}_{p_M} = &\int_{\mathcal{B}} \hat{\boldsymbol{N}}^{\mathsf{T}} S^w \boldsymbol{b}_M : (\nabla^s \boldsymbol{u}^h - \nabla^s \boldsymbol{u}_n^h)\,\mathrm{d}V + \int_{\mathcal{B}} \hat{\boldsymbol{N}}^{\mathsf{T}} \bar{\mathcal{S}}_M (p_M^h - p_{M,n}^h)\,\mathrm{d}V \\ &+ \int_{\mathcal{B}} \hat{\boldsymbol{N}}^{\mathsf{T}} \mathcal{S}_{Mm} (p_m^h - p_{m,n}^h)\,\mathrm{d}V - \Delta t \int_{\mathcal{B}} \boldsymbol{E}_M^{\mathsf{T}} \boldsymbol{q}_{wM}\,\mathrm{d}V \\ &- \Delta t \int_{\mathcal{B}} \hat{\boldsymbol{N}}^{\mathsf{T}} \frac{c_{wM}}{\rho_w}\,\mathrm{d}V - \Delta t \int_{\partial\mathcal{B}_{q_M}} \hat{\boldsymbol{N}}^{\mathsf{T}} \hat{q}_M\,\mathrm{d}A\,,\end{aligned} \tag{87}$$

and for the nanopores, we have

$$\begin{aligned}\boldsymbol{\mathcal{R}}_{p_m} = &\int_{\mathcal{B}} \hat{\boldsymbol{N}}^{\mathsf{T}} \boldsymbol{b}_m : (\nabla^s \boldsymbol{u}^h - \nabla^s \boldsymbol{u}_n^h)\,\mathrm{d}V + \int_{\mathcal{B}} \hat{\boldsymbol{N}}^{\mathsf{T}} \bar{\mathcal{S}}_m (p_M^h - p_{M,n}^h)\,\mathrm{d}V \\ &+ \int_{\mathcal{B}} \hat{\boldsymbol{N}}^{\mathsf{T}} \mathcal{S}_{mm} (p_m^h - p_{m,n}^h)\,\mathrm{d}V - \Delta t \int_{\mathcal{B}} \boldsymbol{E}_m^{\mathsf{T}} \boldsymbol{q}_{wm}\,\mathrm{d}V \\ &- \Delta t \int_{\mathcal{B}} \hat{\boldsymbol{N}}^{\mathsf{T}} \frac{c_{wm}}{\rho_w}\,\mathrm{d}V - \Delta t \int_{\partial\mathcal{B}_{q_m}} \hat{\boldsymbol{N}}^{\mathsf{T}} \hat{q}_m\,\mathrm{d}A\,,\end{aligned} \tag{88}$$

where

$$\begin{aligned}\boldsymbol{E}_M &= \nabla\hat{\boldsymbol{N}} - \frac{\nabla p_M^h}{K_w}\hat{\boldsymbol{N}} \\ \boldsymbol{E}_m &= \nabla\hat{\boldsymbol{N}} - \frac{\nabla p_m^h}{K_w}\hat{\boldsymbol{N}}\end{aligned} \tag{89}$$

and $\hat{\boldsymbol{N}}$ is a row vector of shape functions interpolating the fluid pressures.

The residual equations defined above are highly nonlinear with respect to the nodal solid dispacement and fluid pressures in both the micropores and

nanopores. We thus employ the Newton-Raphson iteration scheme to solve for the unknown variables, which requires construction of an algorithmic tangent operator $\boldsymbol{K}$ for use in the linearized system

$$\begin{bmatrix} \boldsymbol{K}_{11} & \boldsymbol{K}_{12} & \boldsymbol{K}_{13} \\ \boldsymbol{K}_{21} & \boldsymbol{K}_{22} & \boldsymbol{K}_{23} \\ \boldsymbol{K}_{31} & \boldsymbol{K}_{32} & \boldsymbol{K}_{33} \end{bmatrix} \begin{Bmatrix} \delta\boldsymbol{u} \\ \delta\boldsymbol{p}_M \\ \delta\boldsymbol{p}_m \end{Bmatrix} = \begin{Bmatrix} \boldsymbol{\mathcal{R}}_u \\ \boldsymbol{\mathcal{R}}_{p_M} \\ \boldsymbol{\mathcal{R}}_{p_m} \end{Bmatrix}, \tag{90}$$

The submatrices of the tangent operator are presented below. As the surface tension term is small, we neglect its contribution to the tangent operator.

$$\boldsymbol{K}_{11} = \frac{\partial \boldsymbol{\mathcal{R}}_u}{\partial \boldsymbol{u}} = \int_{\mathcal{B}} \boldsymbol{B}^{\mathsf{T}} \mathbb{C}^e \boldsymbol{B} \, \mathrm{d}V \,, \tag{91}$$

where $\mathbb{C}^e$ is the elasticity tensor in matrix form.

$$\begin{aligned} \boldsymbol{K}_{12} = \frac{\partial \boldsymbol{\mathcal{R}}_u}{\partial \boldsymbol{p}_M} = &\int_{\mathcal{B}} \boldsymbol{B}^{\mathsf{T}} \boldsymbol{\xi}_M \hat{\boldsymbol{N}} \, \mathrm{d}V - \int_{\mathcal{B}} \Psi_M \boldsymbol{B}^{\mathsf{T}} \{\boldsymbol{b}_M\} \hat{\boldsymbol{N}} \, \mathrm{d}V \\ &- \int_{\mathcal{B}} r \boldsymbol{N}^{\mathsf{T}} \boldsymbol{g} \hat{\boldsymbol{N}} + \int_{\mathcal{B}} \boldsymbol{N}^{\mathsf{T}} \frac{\partial \bar{\boldsymbol{c}}}{\partial \boldsymbol{p}_M} \, \mathrm{d}V \,, \end{aligned} \tag{92}$$

where

$$\boldsymbol{\xi}_M = \frac{\partial \{\boldsymbol{\sigma}'\}}{\partial S^w} \frac{\partial S^w}{\partial p_M} \,, \quad \Psi = S^w - \frac{\partial S^w}{\partial p_M} p_M^h \,, \quad r = \frac{\partial \rho}{\partial S^w} \frac{\partial S^w}{\partial p_M} \,. \tag{93}$$

The last term on the right-hand side can be expressed as

$$\frac{\partial \bar{\boldsymbol{c}}}{\partial \boldsymbol{p}_M} = \frac{\bar{\alpha} \bar{k} \rho_w}{\mu_w} \Big(- \frac{\boldsymbol{q}_M}{\phi^M} + \frac{\boldsymbol{q}_m}{\phi^m} \Big) \hat{\boldsymbol{N}} - \frac{c_{w,M}}{\phi^M} (\bar{\boldsymbol{K}} \nabla \hat{\boldsymbol{N}} - \boldsymbol{\Phi} \hat{\boldsymbol{N}}) \,. \tag{94}$$

where $\bar{\boldsymbol{K}} = k_{\mathrm{rel}} \boldsymbol{\kappa}_M / \mu_w$ is the matrix of hydraulic conductivity,

$$\boldsymbol{\Phi} = \frac{\partial \bar{\boldsymbol{K}}}{\partial S^w} \frac{\partial S^w}{\partial p_M} \big(\nabla p_M^h - \rho_w \boldsymbol{g} \big) \,. \tag{95}$$

$$\begin{aligned} \boldsymbol{K}_{13} = \frac{\partial \boldsymbol{\mathcal{R}}_u}{\partial \boldsymbol{p}_m} = &\int_{\mathcal{B}} \boldsymbol{B}^{\mathsf{T}} \boldsymbol{\xi}_m \hat{\boldsymbol{N}} \, \mathrm{d}V - \int_{\mathcal{B}} \boldsymbol{B}^{\mathsf{T}} \{\boldsymbol{b}_m\} \hat{\boldsymbol{N}} \, \mathrm{d}V \\ &+ \int_{\mathcal{B}} \boldsymbol{N}^{\mathsf{T}} \frac{\partial \bar{\boldsymbol{c}}}{\partial \boldsymbol{p}_m} \, \mathrm{d}V \,, \end{aligned} \tag{96}$$

where

$$\boldsymbol{\xi}_m = \frac{\partial \{\boldsymbol{\sigma}'\}}{\partial p_m} \,, \tag{97}$$

and

$$\frac{\partial \bar{\boldsymbol{c}}}{\partial \boldsymbol{p}_m} = \frac{\bar{\alpha}\bar{k}\rho_w}{\mu_w}\big(\frac{\boldsymbol{q}_M}{\phi^M} - \frac{\boldsymbol{q}_m}{\phi^m}\big)\hat{\boldsymbol{N}} - \frac{c_{w,m}}{\phi^m}\frac{\boldsymbol{\kappa}_m}{\mu_w}\nabla\hat{\boldsymbol{N}}\,. \tag{98}$$

$$\boldsymbol{K}_{21} = \frac{\partial \boldsymbol{\mathcal{R}}_{p_M}}{\partial \boldsymbol{u}} = \int_{\mathcal{B}} S^w \hat{\boldsymbol{N}}^{\mathsf{T}}\{\boldsymbol{b}_M\}^{\mathsf{T}}\boldsymbol{B}\,\mathrm{d}V \tag{99}$$

$$\begin{aligned}\boldsymbol{K}_{22} = \frac{\partial \boldsymbol{\mathcal{R}}_{p_M}}{\partial \boldsymbol{p}_M} =& \Delta t\int_{\mathcal{B}} \boldsymbol{E}_M^{\mathsf{T}}\bar{\boldsymbol{K}}\nabla\hat{\boldsymbol{N}}\,\mathrm{d}V + \Delta t\int_{\mathcal{B}} \boldsymbol{E}_M^{\mathsf{T}}\boldsymbol{\Phi}\hat{\boldsymbol{N}}\,\mathrm{d}V \\ &+ \int_{\mathcal{B}} \hat{\boldsymbol{N}}^{\mathsf{T}}\Theta_M\hat{\boldsymbol{N}}\,\mathrm{d}V + \Delta t\int_{\mathcal{B}} \hat{\boldsymbol{N}}^{\mathsf{T}}\frac{\bar{\alpha}\bar{k}}{\mu_w}\hat{\boldsymbol{N}}\,\mathrm{d}V\,,\end{aligned} \tag{100}$$

where

$$\begin{aligned}\Theta_M =& \boldsymbol{b}_M : \nabla^s\big(\boldsymbol{u}^h - \boldsymbol{u}_n^h\big)\frac{\partial S^w}{\partial p_M} + \big(p_M^h - p_{M,n}^h\big)\Big(\frac{\mathcal{C}_M}{\partial S^w}\frac{\partial S^w}{\partial p_M} + \frac{\mathcal{S}_{MM}}{\partial S^w}\Big)\frac{\partial S^w}{\partial p_M} \\ &+ \bar{\mathcal{S}}_M + \big(p_m^h - p_{m,n}^h\big)\frac{\partial \mathcal{S}_{Mm}}{\partial S^w}\frac{\partial S^w}{\partial p_M}\,.\end{aligned} \tag{101}$$

$$\boldsymbol{K}_{23} = \frac{\partial \boldsymbol{\mathcal{R}}_{p_M}}{\partial \boldsymbol{p}_m} = \int_{\mathcal{B}} \hat{\boldsymbol{N}}^{\mathsf{T}}\mathcal{S}_{Mm}\hat{\boldsymbol{N}}\,\mathrm{d}V - \Delta t\int_{\mathcal{B}} \hat{\boldsymbol{N}}^{\mathsf{T}}\frac{\bar{\alpha}\bar{k}}{\mu_w}\hat{\boldsymbol{N}}\,\mathrm{d}V\,, \tag{102}$$

$$\boldsymbol{K}_{31} = \frac{\partial \boldsymbol{\mathcal{R}}_{p_m}}{\partial \boldsymbol{u}} = \int_{\mathcal{B}} S^w \hat{\boldsymbol{N}}^{\mathsf{T}}\{\boldsymbol{b}_m\}^{\mathsf{T}}\boldsymbol{B}\,\mathrm{d}V \tag{103}$$

$$\boldsymbol{K}_{32} = \int_{\mathcal{B}} \hat{\boldsymbol{N}}^{\mathsf{T}}\Theta_m\hat{\boldsymbol{N}}\,\mathrm{d}V - \Delta t\int_{\mathcal{B}} \hat{\boldsymbol{N}}^{\mathsf{T}}\frac{\bar{\alpha}\bar{k}}{\mu_w}\hat{\boldsymbol{N}}\,\mathrm{d}V\,, \tag{104}$$

where

$$\begin{aligned}\Theta_m =& \bar{\mathcal{S}}_m + \big(p_M^h - p_{M,n}^h\big)\Big(\frac{\partial \mathcal{C}_m}{\partial S^w}\frac{\partial S^w}{\partial p_M} + \frac{\partial \mathcal{S}_{mM}}{\partial S^w}\Big)\frac{\partial S^w}{\partial p_M} \\ &+ \big(p_m^h - p_{m,n}^h\big)\frac{\partial \mathcal{S}_{mm}}{\partial S^w}\frac{\partial S^w}{\partial p_M}\,.\end{aligned} \tag{105}$$

$$\begin{aligned}\boldsymbol{K}_{33} = \frac{\partial \boldsymbol{\mathcal{R}}_{p_m}}{\partial \boldsymbol{p}_m} =& \Delta t\int_{\mathcal{B}} \boldsymbol{E}_m^{\mathsf{T}}\frac{\boldsymbol{\kappa}_m}{\mu_w}\nabla\hat{\boldsymbol{N}}\,\mathrm{d}V + \int_{\mathcal{B}} \hat{\boldsymbol{N}}^{\mathsf{T}}\mathcal{S}_{mm}\hat{\boldsymbol{N}}\,\mathrm{d}V \\ &+ \Delta t\int_{\mathcal{B}} \hat{\boldsymbol{N}}^{\mathsf{T}}\frac{\bar{\alpha}\bar{k}}{\mu_w}\hat{\boldsymbol{N}}\,\mathrm{d}V\,.\end{aligned} \tag{106}$$

References

[1] Abousleiman YN, Hoang SK, Tran MH (2010). Mechanical characterization of small shale samples subjected to fluid exposure using the inclined direct shear testing device. International Journal of Rock Mechanices and Mining Sciences 47(3):355–367.

[2] Alaoui HM, Giot R, Prêt D, Cosenza P, Hedan S (2023). Development and numerical implementation of a multiscale constitutive law for double-porosity swelling clayey rocks. Computers and Geotechnics 161:105612.

[3] Arndt D, Bangerth W, Blais B, Clevenger TC, Fehling M, Grayver AV, Heister T, Heltai L, Kronbichler M, Maier M, Munch P, Pelteret J, Rastak R, Tomas I, Tuurcksin B, Wang Z, Wells D (2020). The deal. II library, version 9.2. Journal of Numerical Mathematics 28(3):131-146.

[4] Ashworth M, Doster F (2019). Foundations and their practical implications for the constitutive coefficients of poromechanical dual-continuum models. Transport in Porous Media 130(3):699–730.

[5] Askar A, Jin YC (2000). Macroporous drainage of unsaturated swelling soil. Water Resources Research 36(5):1189-97.

[6] Avsar E, Ulusay R, Sonmez H (2009). Assessments of swelling anisotropy of Ankara clay. Engineering Geology 105(1–2):24–31.

[7] Bai M, Elsworth D, Roegiers JC (1993). Multiporosity/multipermeability approach to the simulation of naturally fractured reservoirs. Water Resources Research 29(6):1621–1633.

[8] Bangerth W, Hartmann R, Kanschat G (2007). deal. II—A general-purpose object-oriented finite element library. ACM Transactions on Mathematical Software (TOMS) 33(4): 24-es.

[9] Barenblatt GI, Zheltov IP, Kochina IN. Basic concepts in the theory of seepage of homogeneous liquids in fissured rocks [strata]. Journal of Applied Mathematics and Mechanics 24(5):1286–1303.

[10] Barnaji MJ, Pourafshary P, Rasaie MR (2016). Visual investigation of the effects of clay minerals on enhancement of oil recovery by low salinity water flooding. Fuel 184:826–835.

[11] Barthélémy JF (2009). Effective permeability of media with a dense network of long and micro fractures. Transport in Porous Media 76:153–178.

[12] Bemer E, Longuemare P, Vincké O (2004). Poroelastic parameters of Meuse/Haute Marne argillites: effect of loading and saturation states. Applied Clay Science 26(1–4):359–366.

[13] Berkowitz B (2002). Characterizing flow and transport in fractured geological media: A review. Advances in Water Resources 25(8–12):861–884.

[14] Berkowitz B, Bear J, Braester C (1988). Continuum models for contaminant transport in fractured porous formations. Water Resources Research 24(8):1225–1236.

[15] Berryman JG (2002). Extension of poroelastic analysis to double-porosity materials: New technique in microgeomechanics. Journal of Engineering Mechanics 128(8):840–847.
[16] Bobko C, Ulm FJ (2008). The nano-mechanical morphology of shale. Mechanics of Materials 40:318–337.
[17] Borja RI (2004). Cam-Clay plasticity, Part V: A mathematical framework for three-phase deformation and strain localization analyses of partially saturated porous media. Computer Methods in Applied Mechanics and Engineering, 193(48–51):5301–5338.
[18] Borja RI (2006). On the mechanical energy and effective stress in saturated and unsaturated porous continua. International Journal of Solids and Structures 43(6):1764–1786.
[19] Borja RI, Koliji A (2009). On the effective stress in unsaturated porous continua with double porosity. Journal of the Mechanics and Physics of Solids 57(8):1182–1193.
[20] Borja RI (2013). Plasticity Modeling & Computation, Springer, Berlin-Heidelberg.
[21] Borja RI, Choo J (2016). Cam-Clay plasticity, Part VIII: A constitutive framework for porous materials with evolving internal structure. Computer Methods in Applied Mechanics and Engineering 309:653–679.
[22] Borja RI, Yin Q, Zhao Y (2020). Cam-Clay plasticity. Part IX: On the anisotropy, heterogeneity, and viscoplasticity of shale. Computer Methods in Applied Mechanics and Engineering 360:112695.
[23] Bui BT, Tutuncu AN (2018). Modeling the swelling of shale matrix in unconventional reservoirs. Journal of Petroleum Science and Engineering 165:596-615.
[24] Burstedde C, Wilcox LC, Ghattas O (2011). p4est: Scalable algorithms for parallel adaptive mesh refinement on forests of octrees. SIAM Journal on Scientific Computing 33:1103–1133.
[25] Burton GJ, Pineda JA, Sheng D, Airey D (2015). Microstructural changes of an undisturbed, reconstituted and compacted high plasticity clay subjected to wetting and drying. Engineering Geology 193:363–373.
[26] Cariou S, Dormieux L, Skoczylas F (2013). An original constitutive law for Callovo-Oxfordian argillite, a two-scale double-porosity material. Applied Clay Science 80:18–30.
[27] Casimir HB, Polder D (1948). The influence of retardation on the London-van der Waals forces. Physical Review, 73(4):360.
[28] Chakraborty N, Karpyn ZT, Liu S, Yoon H (2017). Permeability evolution of shale during spontaneous imbibition. Journal of Natural Gas Science and Engineering 38:590–596.
[29] Chapman DL (1913). LI. A contribution to the theory of electrocapillarity. The London, Edinburgh, and Dublin philosophical magazine and journal of science 25(148):475–481.

[30] Chateau X, Dormieux L (2002). Micromechanics of saturated and unsaturated porous media. International Journal for Numerical and Analytical Methods in Geomechanics 26(8):831–844.
[31] Chateau X, Moucheront P, Pitois O (2002). Micromechanics of unsaturated granular media. Journal of Engineering Mechanics 128(8):856–863.
[32] Choo J, Borja RI (2015). Stabilized mixed finite elements for deformable porous media with double porosity. Computer Methods in Applied Mechanics and Engineering 293:131–54.
[33] Choo J, White JA, Borja RI (2016). Hydromechanical modeling of unsaturated flow in double porosity media. International Journal of Geomechanics 16(6):D4016002.
[34] Conti G, Deb R, Matthäi SK, Jenny P (2023). Consistent treatment of shear failure in embedded discrete fracture models using XFVM. International Journal for Numerical and Analytical Methods in Geomechanics, https://doi.org/10.1002/nag.3671.
[35] Cronin MB, Flemings PB, Bhandari AR (2016). Dual-permeability microstratigraphy in the Barnett Shale. Journal of Petroleum Science and Engineering 142:119–128.
[36] Crisci E (2019). Hydro-mechanical response of Opalinus Clay shale: dependency on composition and burial depth. EPFL.
[37] Curtis ME, Sondergeld CH, Ambrose RJ, Rai CS (2012). Microstructural investigation of gas shales in two and three dimensions using nanometer-scale resolution imaging. AAPG Bulletin 96(4):665–677.
[38] d'Onofrio A, Picarelli L, Urciuoli G (2023). The Shear Strength of Two Tectonized Clay Shales. In National Conference of the Researchers of Geotechnical Engineering (pp. 303-310). Cham: Springer Nature Switzerland.
[39] Day-Stirrat RJ, Flemings PB, You Y, Aplin AC, van der Pluijm BA (2012). The fabric of consolidation in Gulf of Mexico mudstones. Marine Geology, 295:77-85.
[40] DeReuil AA, Birgenheier LP, McLennan J (2019). Effects of anisotropy and saturation on geomechanical behavior of mudstone. Journal of Geophysical Research Solid Earth 124(8):8101–8126.
[41] Dormieux L, Kondo D, Ulm FJ (2006). Microporomechanics. John Wiley & Sons.
[42] Douma LA, Dautriat J, Sarout J, Dewhurst DN, Barnhoorn A (2020). Impact of water saturation on the elastic anisotropy of the Whitby Mudstone, United Kingdom. Geophysics 85(1):MR57–MR72.
[43] Dvorak GJ, Benveniste Y. On transformation strains and uniform fields in multiphase elastic media. Proceedings of the Royal Society of London. Series A: Mathematical and Physical Sciences 437(1900):291–310.
[44] Eghbalian M, Pouragha M, Wan R (2019). Micromechanical approach to swelling behavior of capillary-porous media with coupled physics. International Journal for Numerical and Analytical Methods in Geomechanics 43(1):353–380.

[45] Eghbalian M, Wan R, Pouragha M (2022). Multi-scale description of hydro-mechanical coupling in swelling clays. Part I: Nonlinear poroelasticity. Mechanics of Materials 171:104354.
[46] Eghbalian M, Wan R, Pouragha M (2022). Multi-scale description of hydro-mechanical coupling in swelling clays. Part II: Poroplasticity. Mechanics of Materials 171:104357.
[47] Eshelby JD (1961). Elastic inclusion and inhomogeneities. Progress in Solid Mechanics 2:89–140.
[48] Favero V, Ferrari A, Laloui L (2016). On the hydro-mechanical behaviour of remoulded and natural Opalinus Clay shale. Engineering Geology 208:128-35.
[49] Favero V, Ferrari A, Laloui L (2016). Thermo-mechanical volume change behaviour of Opalinus Clay. International Journal of Rock Mechanics and Mining Sciences 90:15-25.
[50] Ferrari A, Favero V, Marschall P, Laloui L (2014). Experimental analysis of the water retention behaviour of shales. International Journal of Rock Mechanics and Mining Sciences 72:61–70.
[51] Ferrari A, Minardi A, Ewy R, Laloui L (2018). Gas shales testing in controlled partially saturated conditions. International Journal of Rock Mechanics and Mining Sciences 107:110–119.
[52] Freeman CM, Moridis G, Ilk D, Blasingame TA (2013). A numerical study of performance for tight gas and shale gas reservoir systems. Journal of Petroleum Science and Engineering 108:22–39.
[53] Freundlich H (1909), Kapillarchemie; eine Darstellung der Chemie der Kolloide und verwandter Gebiete, Akademische Verlagsgesellschaft, Leipzig, Germany.
[54] Gale JF, Laubach SE, Olson JE, Eichhubl P, Fall A (2014). Natural fractures in shale: A review and new observations. AAPG Bulletin 98(11):2165-216.
[55] Gerke HH, Van Genuchten MT (1993). A dual-porosity model for simulating the preferential movement of water and solutes in structured porous media. Water Resources Research 29(2):305–319.
[56] Ghafouri HR, Lewis RW (1996). A finite element double porosity model for heterogeneous deformable porous media. International Journal for Numerical and Analytical Methods in Geomechanics 20(11):831–844.
[57] Ghanbari E, Dehghanpour H (2015). Impact of rock fabric on water imbibition and salt diffusion in gas shales. International Journal of Coal Geology 138:55–67.
[58] Giraud A, Huynh QV, Hoxha D, Kondo D (2007). Effective poroelastic properties of transversely isotropic rock-like composites with arbitrarily oriented ellipsoidal inclusions. Mechanics of Materials 39(11):1006–1024.
[59] Goodarzi M, Rouainia M, Aplin AC (2016). Numerical evaluation of mean-field homogenisation methods for predicting shale elastic response. Computational Geosciences 20:1109–1122.

[60] Griffith CA, Dzombak DA, Lowry GV (2011). Physical and chemical characteristics of potential seal strata in regions considered for demonstrating geological saline CO2 sequestration. Environmental Earth Sciences, 64(4):925–948.
[61] Gu X, Li Y, Hu J, Shi Z, Liang F, Huang M (2022). Elastic shear stiffness anisotropy and fabric anisotropy of natural clays. Acta Geotechnica 17(8):3229–3243.
[62] Guéry AAC, Cormery F, Shao JF, Kondo D (2008). A micromechanical model of elastoplastic and damage behavior of a cohesive geomaterial. International Journal of Solids and structures 45(5):1406-29.
[63] Guéry AAC, Cormery F, Shao JF, Kondo D (2010). A comparative micromechanical analysis of the effective properties of a geomaterial: effect of mineralogical compositions. Computers and Geotechnics 37(5):585–593.
[64] Gutierrez M, Katsuki D, Tutuncu A (2015). Determination of the continuous stress-dependent permeability, compressibility and poroelasticity of shale. Marine and Petroleum Geology 68:614–628.
[65] He J, Rui Z, Ling K (2016). A new method to determine Biot's coefficients of Bakken samples. Journal of Natural Gas Science and Engineering 35:259–264.
[66] Heidug WK, Wong SW (1996). Hydration swelling of water-absorbing rocks: a constitutive model. International journal for numerical and analytical methods in geomechanics 20(6):403-30.
[67] Heroux MA, Willenbring JM (2012). A new overview of the Trilinos project. Scientific Programming 20(2):83–88.
[68] Ho TA, Wang Y, Jové Colón CF, Coker EN (2020). Fast advective water flow through nanochannels in clay interlayers: implications for moisture transport in soils and unconventional oil/gas production. ACS Applied Nano Materials 3(12):11897-905.
[69] Hornby BE, Schwartz LM, Hudson JA (1994). Anisotropic effective-medium modeling of the elastic properties of shales. Geophysics 59(10):1570–1583.
[70] Houben ME, Desbois G, Urai JL (2014). A comparative study of representative 2D microstructures in Shaly and Sandy facies of Opalinus Clay (Mont Terri, Switzerland) inferred form BIB-SEM and MIP methods. Marine and Petroleum Geology 49:143-61.
[71] Hu D, Zhou H, Zhang F, Shao J, Zhang J (2013). Modeling of inherent anisotropic behavior of partially saturated clayey rocks. Computers and Geotechnics 48:29–40.
[72] Ip SCY, Choo J, Borja RI (2021). Impacts of saturation-dependent anisotropy on the shrinkage behavior of clay rocks. Acta Geotechnica 16(11):3381–3400.
[73] Ip SCY, Borja RI (2022). Evolution of anisotropy with saturation and its implications for the elastoplastic responses of clay rocks. Interna-

tional Journal for Numerical and Analytical Methods in Geomechanics 46(1):23–46.
[74] Ip SC, Borja RI (2023). Multiscale interactions of elastic anisotropy in unsaturated clayey rocks using a homogenization model. Acta Geotechnica 15:1–9.
[75] Iwata S, Tabuchi T, Warkentin BP (2020). Soil-water interactions: Mechanisms and applications. CRC Press.
[76] Javadpour F, Fisher D, Unsworth M (2007). Nanoscale gas flow in shale gas sediments. Journal of Canadian Petroleum Technology 46(10), https://doi.org/10.2118/07-10-06.
[77] Jia LY, Chen YG, Ye WM, Cui YJ (2019). Effects of a simulated gap on anisotropic swelling pressure of compacted GMZ bentonite. Engineering Geology 248:155–163.
[78] Kang X, Zou X, Sun HM, Ma XY, Chen RP (2022). Molecular dynamics simulations of microstructure and dynamic shearing behaviors of kaolinite-water-salt system. Applied Clay Science 218:106414.
[79] Karimi-Fard M, Durlofsky LJ, Aziz K (2004). An efficient discrete-fracture model applicable for general-purpose reservoir simulators. SPE Journal 9(02):227–236.
[80] Keller LM, Holzer L, Wepf R, Gasser P (2011). 3D geometry and topology of pore pathways in Opalinus clay: Implications for mass transport. Applied Clay Science 52(1–2):85–95.
[81] Keller LM, Schuetz P, Erni R, Rossell MD, Lucas F, Gasser P, Holzer L (2013). Characterization of multi-scale microstructural features in Opalinus Clay. Microporous and mesoporous materials 170:83-94.
[82] Khalili N, Habte MA, Zargarbashi S (2008). A fully coupled flow deformation model for cyclic analysis of unsaturated soils including hydraulic and mechanical hystereses. Computers and Geotechnics 35(6):872–889.
[83] Khalili N, Selvadurai AP (2003). A fully coupled constitutive model for thermo-hydro-mechanical analysis in elastic media with double porosity. Geophysical Research Letters 30(24), https://doi.org/10.1029/2003GL018838.
[84] Komine H, Ogata N (1996). Prediction for swelling characteristics of compacted bentonite. Canadian Geotechnical Journal 33(1):11–22.
[85] Lai B, Li H, Zhang J, Jacobi D, Georgi D (2016). Water-content effects on dynamic elastic properties of organic-rich shale. SPE J. 21(2):635–647.
[86] Law BE, Curtis JB (2002). Introduction to unconventional petroleum systems. AAPG Bulletin 86(11):1851–1852.
[87] Levin VM (1967). On the thermal expansion coefficients of heterogeneous materials. Mechanics of Solids 1:88–94.
[88] Li D, Wong LN, Liu G, Zhang X (2012). Influence of water content and anisotropy on the strength and deformability of low porosity meta-sedimentary rocks under triaxial compression. Engineering Geology 126:46–66.

[89] Li J, Yin ZY, Cui Y, Hicher PY (2017). Work input analysis for soils with double porosity and application to the hydromechanical modeling of unsaturated expansive clays. Canadian Geotechnical Journal 54(2):173–187.

[90] Liu Y, Borja RI (2022). Time scales in the primary and secondary compression of soils. International Journal for Numerical and Analytical Methods in Geomechanics 46(8):1383–1408.

[91] Liu Y, Burch AC, Bennett KC, Abousleiman Y, Borja RI (2023). Bridging nanoindentation and triaxial creep tests on a shale. Acta Geotechnica 18:6475–6487.

[92] London F (1937). The general theory of molecular forces. Transactions of the Faraday Society 33:8b-26.

[93] Loucks RG, Reed RM, Ruppel SC, Hammes U (2012). Spectrum of pore types and networks in mudrocks and a descriptive classification for matrix-related mudrock pores. AAPG Bulletin 96(6):1071–1098.

[94] Loucks RG, Reed RM, Ruppel SC, Jarvie DM (2009). Morphology, genesis, and distribution of nanometer-scale pores in siliceous mudstones of the Mississippian Barnett Shale. Journal of Sedimentary Research 79(12):848–861.

[95] Louis L, Day-Stirrat R, Hofmann R, Saxena N, Schleicher AM (2018). Computation of effective elastic properties of clay from X-ray texture goniometry data. Geophysics 83(5):MR245–MR261.

[96] Lurie S, Solyaev Y, Shramko K (2018). Comparison between the Mori-Tanaka and generalized self-consistent methods in the framework of anti-plane strain inclusion problem in strain gradient elasticity. Mechanics of Materials 122:133–144.

[97] Lyu Q, Ranjith PG, Long X, Ji B (2016). Experimental investigation of mechanical properties of black shales after CO_2-water-rock interaction. Materials 9(8):663. doi: 10.3390/ma9080663.

[98] Ma XY, Zhu LF, Zou X, Kang X (2023). Investigation of the interface stick-slip friction behavior of clay nanoplatelets by molecular dynamics simulations. Colloids and Surfaces A: Physicochemical and Engineering Aspects 679:132601.

[99] Minaeian V, Dewhurst DN, Rasouli V (2017). Deformational behaviour of a clay-rich shale with variable water saturation under true triaxial stress conditions. Geomechanics for Energy and the Environment 11:1–13.

[100] Minardi A, Crisci E, Ferrari A, Laloui L (2016). Anisotropic volumetric behaviour of Opalinus clay shale upon suction variation. Géotechnique Letters 6(2):144–148.

[101] Mitchell JK, Soga K (2005). Fundamentals of Soil Behavior, Vol. 3, John Wiley & Sons, New York, NY.

[102] Moinfar A, Narr W, Hui MH, Mallison B, Lee SH (2011). Comparison of discrete-fracture and dual-permeability models for multiphase flow in

naturally fractured reservoirs. In: SPE Reservoir Simulation Conference pp. SPE-142295). SPE.

[103] Monfared M, Sulem J, Delage P, Mohajerani M (2014). Temperature and damage impact on the permeability of Opalinus Clay. Rock Mechanics and Rock Engineering 47:101–110.

[104] Mori T, Tanaka K (1973). Average stress in matrix and average elastic energy of materials with misfitting inclusions. Acta Metallurgica 21(5):571–574.

[105] Mualem Y (1976). A new model for predicting the hydraulic conductivity of unsaturated porous media. Water Resources Research 12(3):513–522.

[106] Murad MA, Moyne C (2008). A dual-porosity model for ionic solute transport in expansive clays. Computational Geosciences 12:47–82.

[107] Nemat-Nasser S, Hori M (2013). Micromechanics: overall properties of heterogeneous materials. Elsevier.

[108] Neuzil CE (2013). Can shale safely host US nuclear waste?. Eos, Transactions American Geophysical Union 94(30):261–262.

[109] Noorishad J, Mehran M (1982). An upstream finite element method for solution of transient transport equation in fractured porous media. Water Resources Research 18(3):588–596.

[110] Novich BE, Ring TA (1984). Colloid stability of clays using photon correlation spectroscopy. Clays and Clay Minerals 32(5):400–406.

[111] Pan B, Yin X, Ju Y, Iglauer S (2021). Underground hydrogen storage: Influencing parameters and future outlook. Advances in Colloid and Interface Science 294:102473.

[112] Pankow JF, Johnson RL, Hewetson JP, Cherry JA (1986). An evaluation of contaminant migration patterns at two waste disposal sites on fractured porous media in terms of the equivalent porous medium (EPM) model. Journal of Contaminant Hydrology 1(1–2):65–76.

[113] Pardoen B, Bésuelle P, Dal Pont S, Cosenza P, Desrues J (2020). Accounting for small-scale heterogeneity and variability of clay rock in homogenised numerical micromechanical response and microcracking. Rock Mechanics and Rock Engineering 53:2727–2746.

[114] Parnell WJ (2016). The Eshelby, Hill, moment and concentration tensors for ellipsoidal inhomogeneities in the Newtonian potential problem and linear elastostatics. Journal of Elasticity 125(2):231–294.

[115] Philipp T, Amann-Hildenbrand A, Laurich B, Desbois G, Littke R, Urai JL (2017). The effect of microstructural heterogeneity on pore size distribution and permeability in Opalinus Clay (Mont Terri, Switzerland): insights from an integrated study of laboratory fluid flow and pore morphology from BIB-SEM images. Geological Society, London, Special Publications 454(1):85-106.

[116] Pichler B, Hellmich C (2010). Estimation of influence tensors for eigenstressed multiphase elastic media with nonaligned inclusion phases of ar-

bitrary ellipsoidal shape. Journal of Engineering Mechanics 136(8):1043–1053.

[117] Revil A, Lu N (2013). Unified water isotherms for clayey porous materials. Water Resources Research 49(9):5685–5699.

[118] Saba S, Barnichon JD, Cui YJ, Tang AM, Delage P (2014). Microstructure and anisotropic swelling behaviour of compacted bentonite/sand mixture. Journal of Rock Mechanics and Geotechnical Engineering 6(2):126–132.

[119] Salager S, Nuth M, Ferrari A, Laloui L (2013). Investigation into water retention behaviour of deformable soils. Canadian Geotechnical Journal 50(2):200–208.

[120] Sánchez M, Gens A, Villar MV, Olivella S (2016). Fully coupled thermo-hydro-mechanical double-porosity formulation for unsaturated soils. International Journal of Geomechanics 16(6):D4016015.

[121] Sarout J, Esteban L, Delle Piane C, Maney B, Dewhurst DN (2014). Elastic anisotropy of Opalinus Clay under variable saturation and triaxial stress. Geophysical Journal International 198(3):1662–1682.

[122] Semnani SJ, White JA, Borja RI (2016). Thermoplasticity and strain localization in transversely isotropic materials based on anisotropic critical state plasticity. International Journal for Numerical and Analytical Methods in Geomechanics 40(18):2423–2449.

[123] Semnani SJ, White JA (2020). An inelastic homogenization framework for layered materials with planes of weakness. Computer Methods in Applied Mechanics and Engineering 370:113221.

[124] Sevostianov I, Vernik L (2021). Micromechanics-based rock-physics model for inorganic shale. Geophysics 86(2):MR105–MR116.

[125] Shen WQ, Shao JF, Kondo D, Gatmiri B (2012). A micro–macro model for clayey rocks with a plastic compressible porous matrix. International journal of plasticity 36:64-85.

[126] Siegesmund S, Popp T, Kaufhold A, Dohrmann R, Gräsle W, Hinkes R, Schulte-Kortnack D (2017). Seismic and mechanical properties of Opalinus Clay: comparison between sandy and shaly facies from Mont Terri (Switzerland). Environmental earth sciences 71:3737-49.

[127] Sone H, Zoback MD (2013). Mechanical properties of shale-gas reservoir rocks—Part 1: Static and dynamic elastic properties and anisotropy. Geophysics 78(5):D381–D392.

[128] Song X, Borja RI (2014). Mathematical framework for unsaturated flow in the finite deformation range. International Journal for Numerical Methods in Engineering 97(9):658–682.

[129] Song X, Borja RI (2014). Finite deformation and fluid flow in unsaturated soils with random heterogeneity. Vadose Zone Journal 13(5):vzj2013.07.0131.

[130] Swan G, Cook J, Bruce S, Meehan R (1989). Strain rate effects in Kimmeridge Bay shale. InInternational Journal of Rock Mechanics and Min-

ing Sciences & Geomechanics Abstracts Vol. 26, No. 2, pp. 135-149. Pergamon.

[131] Tuller M, Or D (2001). Hydraulic conductivity of variably saturated porous media: Film and corner flow in angular pore space. Water Resources Research 37(5):1257–1276.

[132] Ulm FJ, Delafargue A, Constantinides G (2005). Experimental microporomechanics. In Applied micromechanics of porous materials (pp. 207–288). Springer, Vienna.

[133] Valès F, Minh DN, Gharbi H, Rejeb A (2004). Experimental study of the influence of the degree of saturation on physical and mechanical properties in Tournemire shale (France). Applied Clay Science 26:197–207.

[134] Valliappan S, Khalili-Naghadeh N (1990). Flow through fissured porous media with deformable matrix. International Journal for Numerical Methods in Engineering 29(5):1079–1094.

[135] Van Genuchten MT (1980). A closed-form equation for predicting the hydraulic conductivity of unsaturated soils. Soil Science Society of America Journal 44:892–898.

[136] Vasin RN, Wenk HR, Kanitpanyacharoen W, Matthies S, Wirth R (2013). Elastic anisotropy modeling of Kimmeridge shale. Journal of Geophysical Research: Solid Earth 118(8):3931–3956.

[137] Vernik L, Nur A (1992). Ultrasonic velocity and anisotropy of hydrocarbon source rocks. Geophysics 57(5):727–735.

[138] Vernik L, Anantharamu V (2020). Estimating the elastic properties of mica and clay mineralsElastic properties of mica and clay minerals. Geophysics, 85(2):MR83–MR95.

[139] Villar MV, Lloret AJ (2004). Influence of temperature on the hydromechanical behaviour of a compacted bentonite. Applied Clay Acience 26(1-4):337–350.

[140] Vincké O, Longuemare P, Boutéca M, Deflandre JP (1998). Investigation of the poromechanical behavior of shales in the elastic domain. In SPE/ISRM Rock Mechanics in Petroleum Engineering (pp. SPE-47589). SPE.

[141] Wenk HR, Lonardelli I, Franz H, Nihei K, Nakagawa S (2007). Preferred orientation and elastic anisotropy of illite-rich shale. Geophysics, 72(2):E69–E75.

[142] Wenk H-R, Voltolini M, Mazurek M, Van Loon LR, Vinsot A (2008). Preferred orientations and anisotropy in shales: Callovo-Oxfordian shale (France) and Opalinus Clay (Switzerland). Clays and Clay Minerals 56:285–306.

[143] White JA, Borja RI (2008). Stabilized low-order finite elements for coupled solid-deformation/fluid-diffusion and their application to fault zone transients. Computer Methods in Applied Mechanics and Engineering 197:4353–4366.

[144] Wild KM, Wymann LP, Zimmer S, Thoeny R, Amann F (2015). Water retention characteristics and state-dependent mechanical and petrophysical properties of a clay shale. Rock Mechanics and Rock Engineering, 48(2):427–439.
[145] Wong LNY, Maruvanchery V, Liu G (2016). Water effects on rock strength and stiffness degradation. Acta Geotechnica, 11(4):713–737.
[146] Wong RC, Wang EZ (1997). Three-dimensional anisotropic swelling model for clay shale—a fabric approach. International Journal of Rock Mechanics and Mining Sciences 34(2):187–198.
[147] Yang DS, Bornert M, Chanchole S, Gharbi H, Valli P, Gatmiri B (2012). Dependence of elastic properties of argillaceous rocks on moisture content investigated with optical full-field strain measurement techniques. International Journal of Rock Mechanics and Mining Sciences, 53:45–55.
[148] Yang J, Fall M (2021). A dual porosity poroelastic model for simulation of gas flow in saturated claystone as a potential host rock for deep geological repositories. Tunnelling and Underground Space Technology 115:104049.
[149] Yanuka M, Dullien FAL, Elrick DE (1986). Percolation processes and porous media: I. Geometrical and topological model of porous media using a three-dimensional joint pore size distribution. Journal of Colloid and Interface Science, 112(1):24–41.
[150] Yin ZY, Chang CS, Hicher PY, Karstunen M (2009). Micromechanical analysis of kinematic hardening in natural clay. International Journal of Plasticity 25(8):1413-35.
[151] Yurikov A, Lebedev M, Pervukhina M, Gurevich B. (2019). Water retention effects on elastic properties of Opalinus shale. Geophysical Prospecting, 67(4):984–996.
[152] Zhang CL, Wieczorek K, Xie ML (2010). Swelling experiments on mudstones. Journal of Rock Mechanics and Geotechnical Engineering 2(1):44–51.
[153] Zhang F, Xie SY, Hu DW, Shao JF, Gatmiri B (2012). Effect of water content and structural anisotropy on mechanical property of claystone. Applied Clay Science 69:79–86.
[154] Zhang J, Bai M, Roegiers JC (2003). Dual-porosity poroelastic analyses of wellbore stability. International Journal of Rock Mechanics and Mining Sciences 40(4):473–483.
[155] Zhang J, Roegiers JC (2005). Double porosity finite element method for borehole modeling. Rock Mechanics and Rock Engineering 38:217–242.
[156] Zhang Q, Borja RI (2021). Poroelastic coefficients for anisotropic single and double porosity media. Acta Geotechnica 16(10):3013–3025.
[157] Zhang Q, Choo J, Borja RI (2019). On the preferential flow patterns induced by transverse isotropy and non-Darcy flow in double porosity media. Computer Methods in Applied Mechanics and Engineering 353:570–592.

[158] Zhang Q, Fan X, Chen P, Ma T, Zeng F (2020). Geomechanical behaviors of shale after water absorption considering the combined effect of anisotropy and hydration. Engineering Geology 269:105547.

[159] Zhang Q, Wang ZY, Yin ZY, Jin YF (2022). A novel stabilized NS-FEM formulation for anisotropic double porosity media. Computer Methods in Applied Mechanics and Engineering 401:115666.

[160] Zhang Z, Song X (2022). Nonequilibrium molecular dynamics (NEMD) modeling of nanoscale hydrodynamics of clay-water system at elevated temperature. International Journal for Numerical and Analytical Methods in Geomechanics 46(5):889-909.

[161] Zhang WH, Fu LY, Zhang Y, Jin WJ (2016). Computation of elastic properties of 3D digital cores from the Longmaxi shale. Applied Geophysics 13(2):364–374.

[162] Zhang Y, Xie L, Zhao P, He B (2020). Study of the quantitative effect of the depositional layering tendency of inclusions on the elastic anisotropy of shale based on two-step homogenization. Geophysical Journal International, 220(1):174–189.

[163] Zhao Y, Borja RI (2021). Anisotropic elastoplastic response of double-porosity media. Computer Methods in Applied Mechanics and Engineering 380:113797.

[164] Zhao Y, Borja RI (2022). A double-yield-surface plasticity theory for transversely isotropic rocks. Acta Geotechnica 17(11):5201–5221.

[165] Zhao Y, Semnani SJ, Yin Q, Borja RI (2018). On the strength of transversely isotropic rocks. International Journal for Numerical and Analytical Methods in Geomechanics 42(16):1917–1934.

[166] Zhong Y, Zhou A, Du J, Teng J, Shen SL (2023). Modified Kozeny-Carman equation for estimating hydraulic conductivity in nanoscale pores of clayey soils with active surfaces. Journal of Hydrology 626:130209.

[167] Zhou Z-h, Wang H-n, Jiang M-j (2021). Macro- and micro-mechanical relationship of the anisotropic behaviour of a bonded ellipsoidal particle assembly in the elastic stage. Acta Geotechnica 16:3899–3921.